UNIVERSITAT POLITÈCNICA DE VALÈNCIA

CAMPUS D'ALCOI

Elaboration of a rotor and the mechanical shaft of a Direct Drive Wind Turbine

---

MEMORIA PRESENTADA POR:

Benjamin Brunke

GRADO DE *Ingeniería Mecánica*

Convocatoria de defensa: *Febrero/Marzo 2021*

Content Chart

Executive Summary

The objective of this project is the design of an offshore wind turbine starting by finding a location for its emplacement and analyzing the ambient conditions of wind and sea. Once this is established the rotor will be dimensioned for optimum extraction of energy, this includes an evaluation of power extraction of the wind and analysis and the analysis of the wake the rotor generates downstream, and the deformations the blade suffers due to the aerodynamic stresses. Within these loading conditions the shaft that transmits the energy extracted from the wind onto the electric generator is designed. This includes cylindrical contour of the shaft, along with the selection and calculations of the appropriate bearings for these exceptionally high operating circumstances. Finally, the cost of this entire part is estimated using generalized expressions to determine wind turbine cost.

Key Words

Wind energy, Wind turbine, Offshore, Rotor blade, Airfoil, NACA, Shaft, Bearing, Transmission

Preliminary

In this part the symbology which is used throughout the entire document is defined and developed. All these variables may contain subindexes to refer to a certain object or enumeration when there are several.

A	Area
a	Axial induction factor
a’	Angular Induction factor
B	Number of blades
C_P	Power coefficient
c	Chord length
c’	Velocity Weibull coefficient
D	Diameter
E	Elastic Modulus
F	Force
F’	Prandtl’s tip loss factor
f	Prandtl’s tip loss geometry factor
G	Shear Modulus
g	Gravity
H	Hours
h	Thickness
I	Inertia
i	Transmission ration
k	Dimensionless Weibull coefficient
L	Length
M	Moment of force
m	Mass
N	Nominal revolution range
P	Power
p	Pressure
$\mathcal{P}$	Probability
Q	Torque
q	Distributed Load
R	Blade Radius
r	Radial Position
Re	Reynolds number
T	Thrust
t	Time
T^a	Temperature
V	Volume
v	Velocity
v_∞	Atmospheric wind speed
z	Height
z’	Surface roughness height
α	Local angle of attack
β	Angle of Principal Inertia axis
γ	Wake Entrainment Constant

ε	True normal strain
η	Efficiency
θ_{CP}	Pitch angle of the blade
θ_T	Local twist angle of the rotor segment
κ	Viscosity Ratio
λ	Tip speed ratio
μ	Friction Coefficient
ρ	Density
σ	Normal Stress
τ	Tangential Stress
ϕ	Angle between velocity and plane of rotation
ψ	Correction function for atmospheric stability
Ω	Rotational speed of the rotor
ω'	Rotational speed of the wake
ω	Rotational speed of mechanical parts

Introduction and Objectives

This project is oriented to set the ground stone to build a offshore wind park to contribute to renewable energy obtention for the Spanish electrical system. Thus, the wind in the different offshore areas of Spain is studied and a rotor and mechanical system is designed for this purpose. The objectives of this project can therefore be summed up as:

- Analyze the Eolic circumstances offshore the coast of Spain
- Characterize the wind according to a Weibullian statistical model
- Select the geometry of the rotor blades
- Study the performance of the rotor in these wind conditions
- Design the transmission shaft of the turbine

1. Selection and Analysis of the Location

When it comes to possible offshore locations for wind turbines, Spain offers two major possibilities within the Iberian Peninsula, the north coast including the Cantabrian Sea and the Atlantic Ocean and the south/south east coast heading into the Mediterranean Sea. Due to their nature, restricted and/or environmentally protected areas are immediately excluded from the possible sites. These are as shown in Figure 1.1, which is a map elaborated by the Europarc Foundation [1]. Furthermore, is it to consider leaving a safety distance of at least 3.5 nautical miles or the equivalent, six thousand five hundred meters to commercially transited maritime routes according to the risk classification realized by the MCA in 2004.

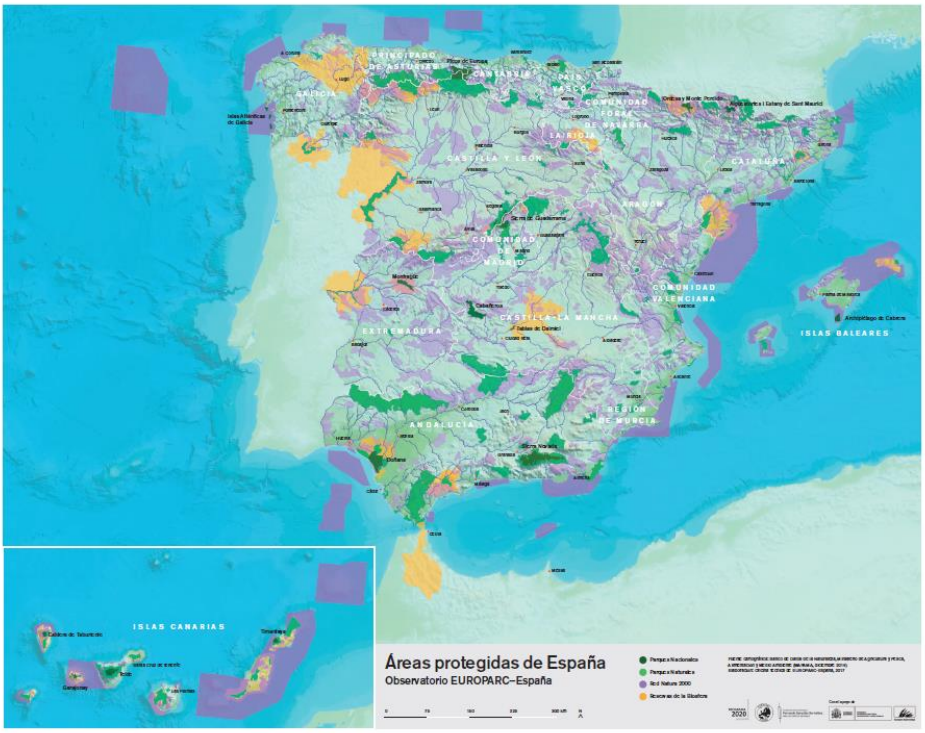

Figure 1.1 Environmentally protected areas [1]

Determined in which areas the construction of a wind park is prevented by the intervention of environmental protecting laws the most optimum site is selected by overlapping and trading off different aspects that influence the construction and/or power obtention at the site. These factors are: Power density, statistical daily operational hours, and vessel traffic. Depth of the seabed can be dismissed due to, in case this factor was limiting, the supporting structure could be replaced employing floating structures, these kind of structures come with the benefit of allowing additional mechanism of energy storage and additional energy supply in moments of excessive or shortage of supply, respectively, however, they come with the drawback of requiring a higher initial economic investment along with associated higher maintenance costs implied by higher amounts of components that could cause a potential failure.

Next points of analysis are the wind power density and operational hours. To conduct a preselection, data out of the energy atlas of the IDAE [2]. These concepts are mainly connected to project economics. Textbook values establish the border value for

rentability for an offshore wind park to be above four hundred Watts per square meter. Figure 1.2 shows a map depicting the wind power density on the sea within Spanish borders and Figure 1.3 the available hours. Both figures are set a reference height of eighty meters above sea level.

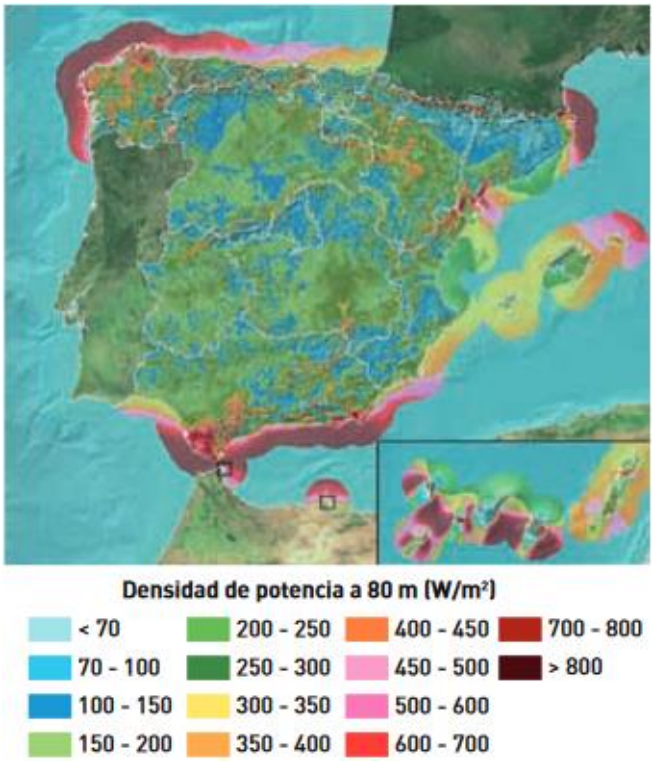

Figure 1.2 Power Density at 80 meters [2]

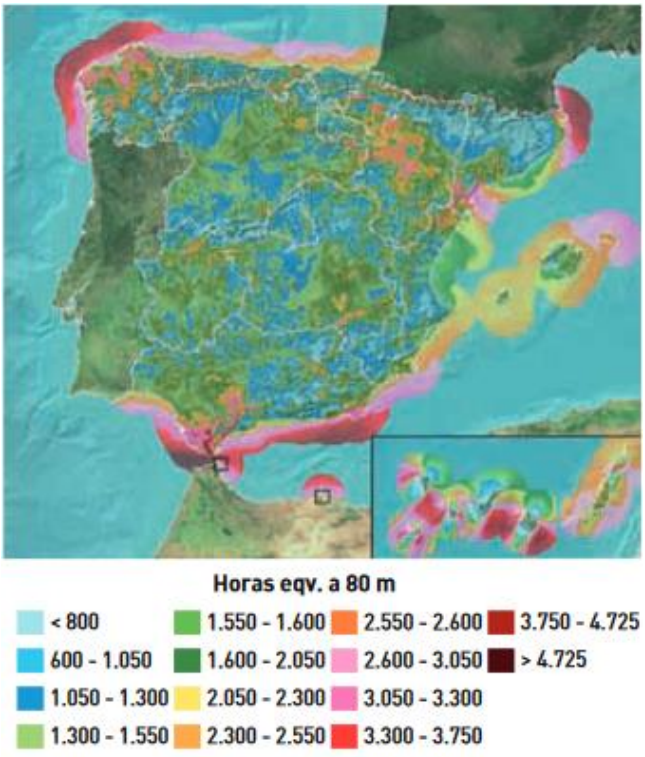

Figure 1.3 Operational yearly hours at 80 meters [2]

Last possible limitation factor is the vessel traffic. Since winds parks take off a lot of space that becomes restricted to vessel traffic for safety reasons, it is to pick an area in which the amount of traffic that needs to be redirected, if any, is as small as possible. The traffic density for the North coast is shown in Figure 1.5 and the density for the Mediterranean coast is shown in Figure 1.6. This information is retrieved from the traffic statistic database of the international maritime traffic tracking tool [3].

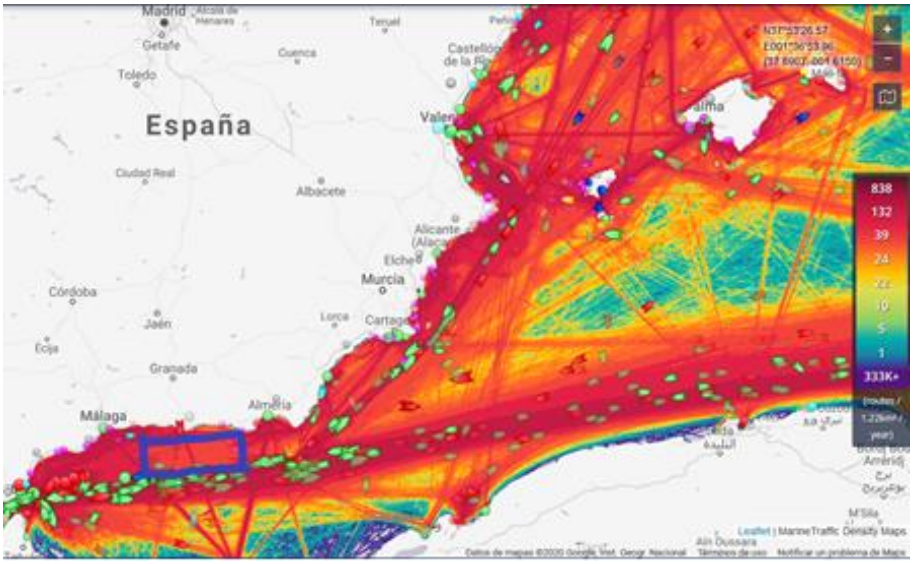

Figure 1.5: Statistical vessel traffic Spanish Mediterranean Sea [3]

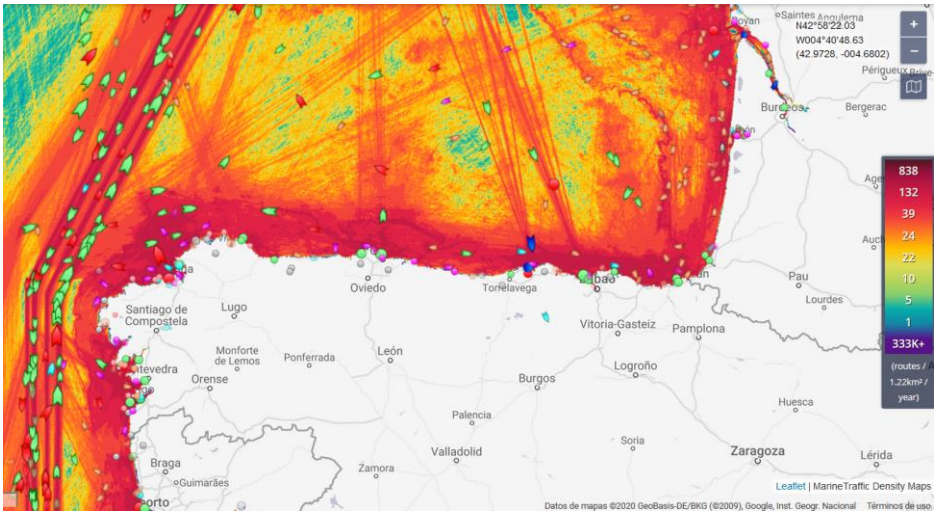

Figure 1.6 Statistical vessel traffic Spanish Atlantic Ocean [3]

Observing the graph of power density and overlapping it with the operational yearly hours, the main options are the Galicians coast, the Catalonian coast at the border to France and the coast of Andalusia east of the Strait of Gibraltar. After overlaying these regions with the Europarc Map, Figure 1.1, it is, that the site considered to be best for this project is the area marked in blue in Figure 1.5 in the Alboran Sea between the coastal equivalent of Malaga and Almeria. The proper wind analysis follows in the next chapter of this document.

2. Analysis of the wind data

Having picked the site which provides the best possible conditions for offshore wind turbines a detailed analysis of the wind is conducted, this includes average and maximum wind speed, frequencies, directions, and the roughness. For this historical data is obtained from measure points located in buoys belonging to the Spanish national institute of oceanography. These measure points are Simar 2046078, Simar 2046076, Simar 2040078 and Simar 2040076.

2.1 Roughness

For the roughness length, z', the textbook value is used. This value is estimated to be approximately 0.0002 [4] meters on open water. On the open sea, as the wind speed increases this roughness value also increases however, the variation is small enough to be considered negligible. Given the boundary layer theory wind profiles are observed to change depending on day and night. This is due to heat flux changes; however, this effect does not happen on open sea therefore the atmospheric stability correction coefficient, $\psi = 0$. This then means that the wind profile as a function of height can be determined with equation 2.1.1, being z_r the data references height, in this case 0.5 meters which is the height of the anemometers on the buoys and evolve as shown in Figure 2.1.1, being the v_r two meters per second.

$$v(z) = v_r \frac{\ln(z/z')}{\ln(z_r/z')} \qquad \text{(Eq 2.1.1)}$$

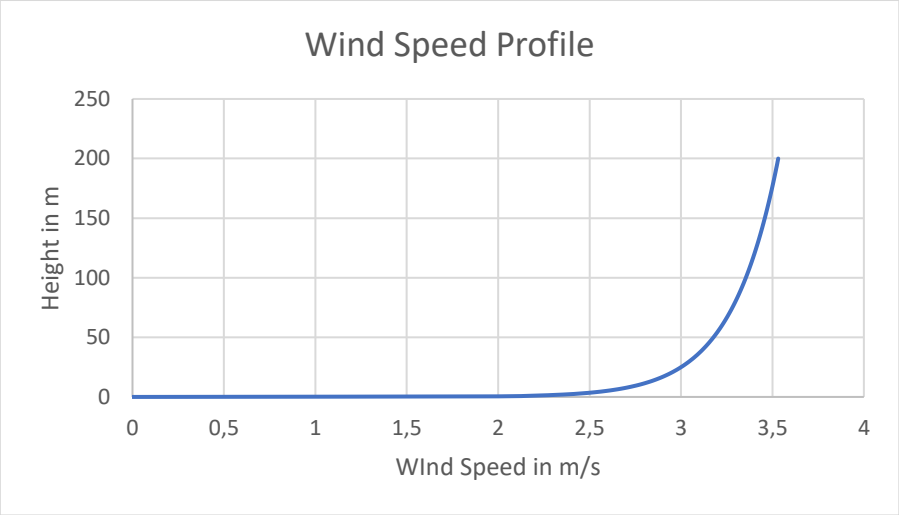

Figure 2.1.1 Wind Profile

2.2 Maximum wind speeds measured and their directions.

Although these wind speeds tend to exceed the cut-out speed of the wind turbine, which means that the blades will be rotated out of the wind, reducing the lift the wind generates to a minimum and the brake applied and will therefore not be considered in the calculations of the energy transforming mechanism. However, these calculations become very important for the structural elements of the turbine.

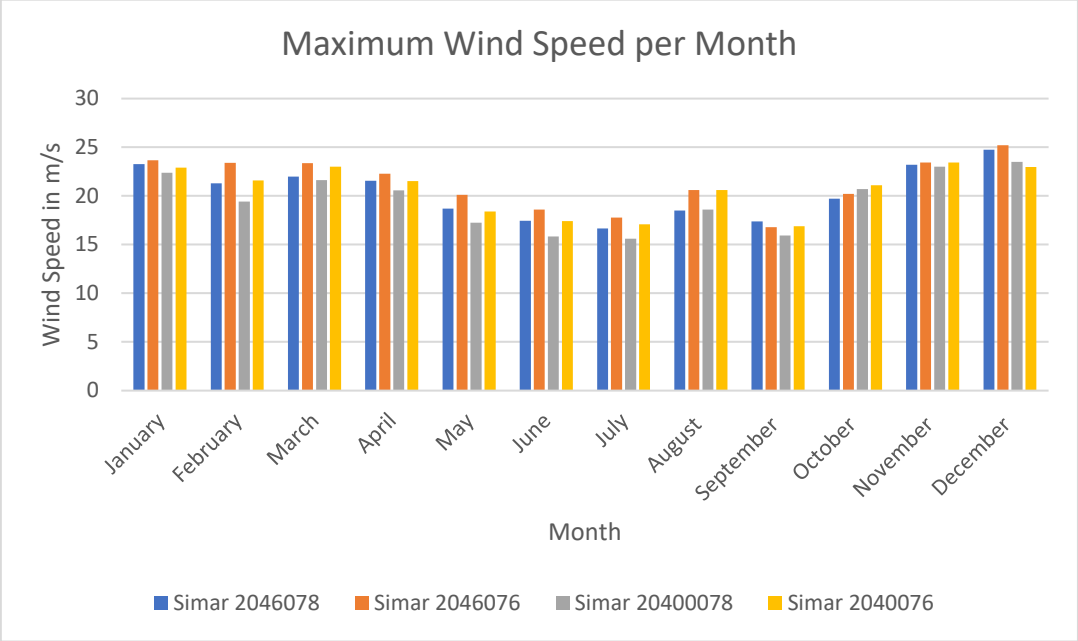

Figure 2.2.1 Maximum Average Speeds per month

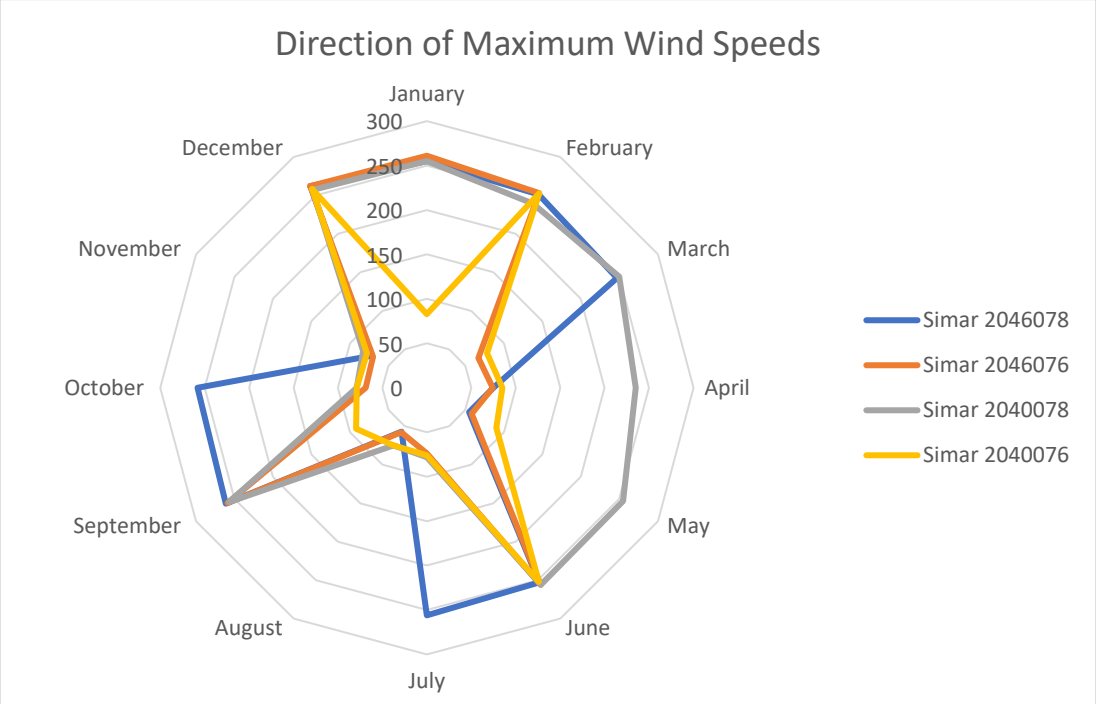

Figure 2.2.2 Direction of Maximum Speeds

2.3 Frequencies of winds and Probabilities

To determine the operational hours and the respective speeds the statistical Weibull method is employed. Initially the constants *c* and *k* are determined with the graphical method based on the logarithmic scale as displayed in Figure 2.3.1. Then the *c* and *k* value are calculated for design hub height and the converge criteria *n'* is calculated to confirm that the values are coherent. For Simar 2046078 this is. Based on data X in Appendix Y. Developing the *y* result using Eq. 2.2.1.

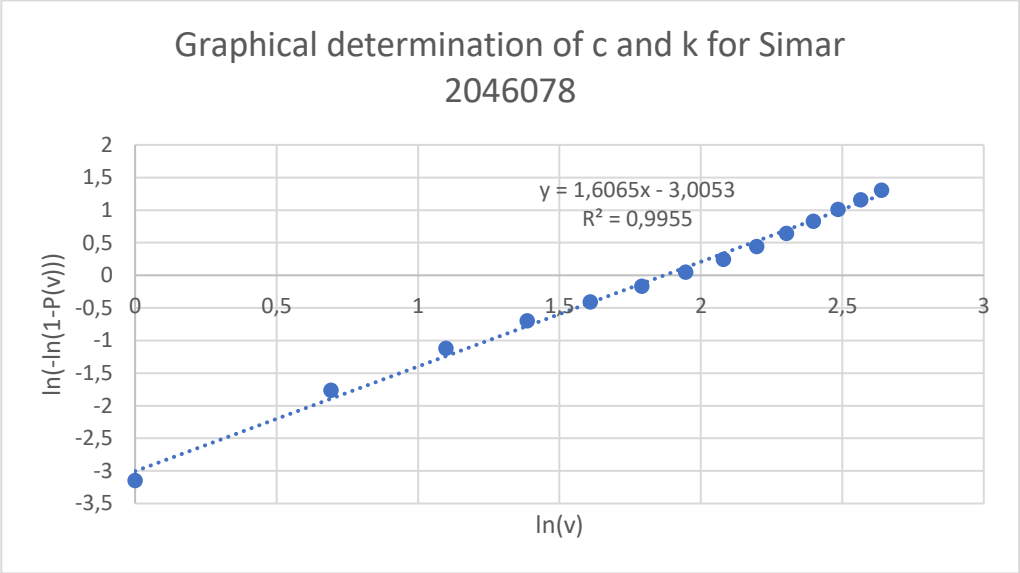

Figure 2.3.1 Weibull Progression

Using this linear model as a linear equation (y = mx - b) this leads to:

$$ln(-ln(1 - P(v))) = k\ ln(v)\ - k\ ln(c) \qquad \text{(Eq 2.3.1)}$$

Established this relationship, the slope of the linear regression line *m* can is the coefficient *k*. Knowing the value of *k* the value of *c* can be computed out of the term *b* for it is the equivalent of *k ln(c)*. Transposing these values than to the hub height using Eq. 2.3.2 for *k* and Eq. 2.3.3 for *c*. Eq. 2.3.4 determines the value n. The results of all the buoys can be red in table 2.3.1

$$k = k_r \frac{(1 - 0.088 \ln(z_r/10))}{(1 - 0.088 \ln(z/10))} \qquad \text{(Eq 2.3.2)}$$

$$c = c_r(\frac{z}{z_r})^n \qquad \text{(Eq 2.3.3)}$$

$$n = \frac{(0.37 - 0.088 \ln(c_r))}{(1 - 0.088 \ln(z_r/10))} \qquad \text{(Eq 2.3.4)}$$

Table 2.3.1 Values of *c* and *k*

	Simar 2046078	Simar 2046076	Simar 2040078	Simar 2040076
kref	1.6065	1.6252	1.5297	1.611
cref	6.493	7.3171	5.9382	6.7373
n	0.1625	0.1542	0.1687	0.1599
k	2.5981	2.6283	2.4739	2.6054
c	15.8523	17.8317	14.9732	16.418

For all buoys n < 0.2 so convergency criteria is accomplished and results can be considered coherent. These values can now be used to calculate the probability of the wind speed being between cut-in and cut-out speed also using the Weibull statistical method with Eq. 2.3.5.

$$P(v_{CI} < v < v_{CO}) = exp(-(v_{CI}/c)^k) - exp(-(v_{CO}/c)^k) \qquad \text{(Eq 2.3.5)}$$

This value for each buoy is as represented in Table 2.3.2 which than multiplied by 24 and 365 determines the statistical operational hours per year.

Table 2.3.2 Probabilities and hours per year

Buoy	P(v)	h/y
Simar 2046078	0.82	7250
Simar 2046076	0.73	6413
Simar 2040078	0.85	7522
Simar 2040076	0.80	7010

Outlining this data showing the statistical hours of each speed per day is shown in figure 2.3.2.

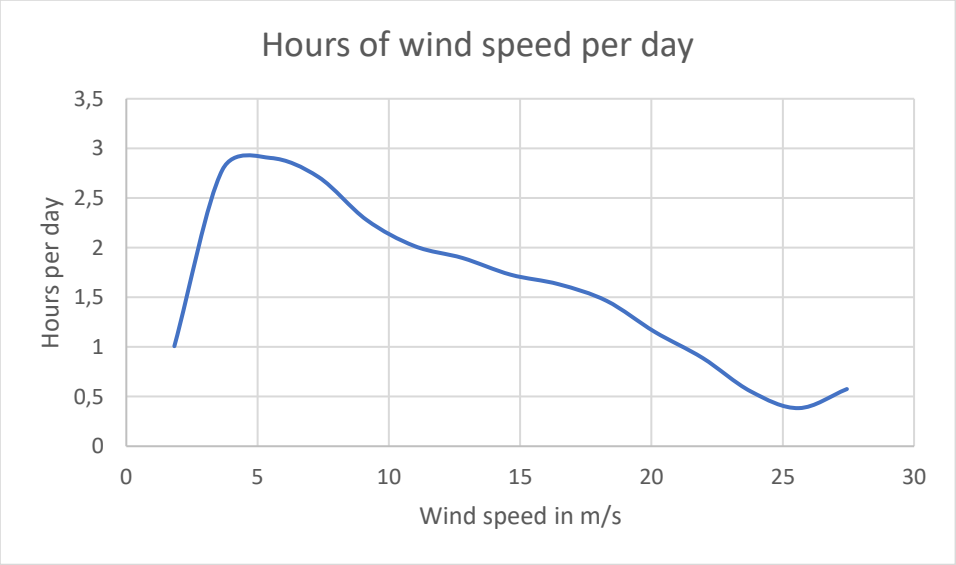

Figure 2.3.2 Hours of wind speed per day

3. Rotor

In this section the rotor of the wind turbine is analyzed. Initially laying out its compound shape and posteriorly the performance analysis under several wind conditions as well as the individual blades responses to the loads they are submitted to in different loading scenarios guaranteeing the static and fatigue resistance with the established safety factors for each scenario. According to the NREL, for a 95% survival rate the safety factor for ultimate static load should be between 2.45 and 2.95 whereas the fatigue safety factor should be between 1.48 and 1.95 [5]. Given the high grade of uncertainty there is in alternating factors such as turbulences, a probabilistic design approach is considered unviable.

3.1 Shape of the rotor

For the airfoil design an already established pre-design of an example wind turbine by the NREL is used. This is a complex airfoil, which means it is integrated by the combination of several simple ones. Source of this can be found in the technical report of the NREL, NREL/TP-500-38060 from February 2009 [6]. This leads to the geometry properties exposed in chart 3.1.1 and drawn in CAD in Figure 3.1.8 Since the turbine is operating under different wind conditions, some minor alterations were necessary to fit structural requirements without striving to faraway of the performance. To reduce the excessive bending at the tip, the tip geometry has been changed to an airfoil with higher drag than lift. The justification of that is developed further ahead in part 3.3. The CAD of the modified geometry is exposed in Figure 3.1.11 whereas table 3.1.X includes the modified data of the airfoil. Maximum power that an ideal wind turbine with an actuator disk the size of the rotor is given by the Betz limit and plotted in figure 3.1.9

Table 3.1.1 Reference Rotor Geometry

Node	Rnodes (m)	r/R	AeroTwist Theta T(º)	DRNodes (m)	Chord Length(m)	Airfoil Type
1	2.8667	0.0455	13.308	2.7333	3.542	Cylinder 1
2	5.6000	0.0888	13.308	2.7333	3.854	Cylinder 1
3	8.3333	0.1322	13.308	2.7333	4.167	Cylinder 2
4	11.7500	0.1865	13.308	4.1000	4.557	DU 99 W 405 LM
5	15.8500	0.2515	11.480	4.1000	4.652	DU 99 W 350
6	19.9500	0.3166	10.162	4.1000	4.458	DU 99 W 350
7	24.0500	0.3817	9.011	4.1000	4.249	DU 97 W 300 LM
8	28.1500	0.4468	7.795	4.1000	4.007	DU 91 W2-250
9	32.2500	0.5119	6.544	4.1000	3.748	DU 91 W2-250
10	36.3500	0.5769	5.361	4.1000	3.502	DU 93-W-210 LM
11	40.4500	0.6420	4.188	4.1000	3.256	DU 93-W-210 LM
12	44.5500	0.7071	3.125	4.1000	3.010	NACA 64-618
13	48.6500	0.7722	2.319	4.1000	2.764	NACA 64-618
14	52.7500	0.8373	1.526	4.1000	2.518	NACA 64-618
15	56.1667	0.8915	0.863	2.7333	2.313	NACA 64-618
16	58.9000	0.9349	0.370	2.7333	2.086	NACA 64-618
17	61.6333	0.9783	0.106	2.7333	1.419	NACA 64-618

At continuation the figures 3.1.1 – 3.1.7 represent the different profiles by a points which are then used in the CAD model to generate a surface

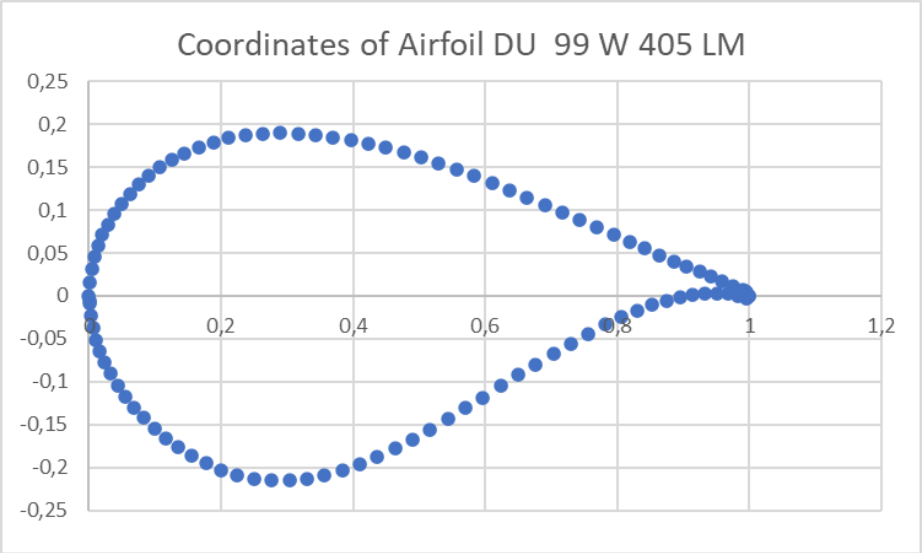

Figure 3.1.1 DU 99 W 405 LM

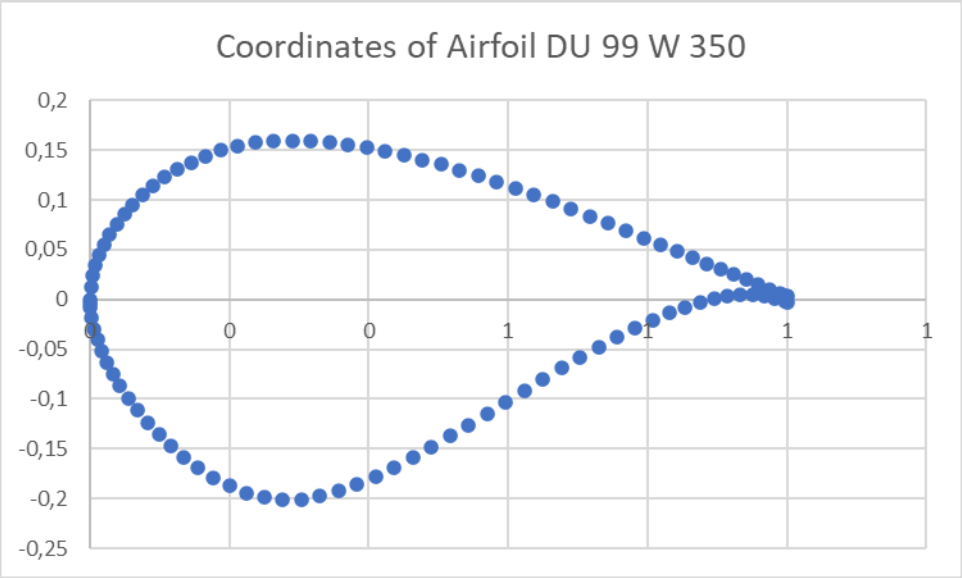

Figure 3.1.2 DU 99 W 350

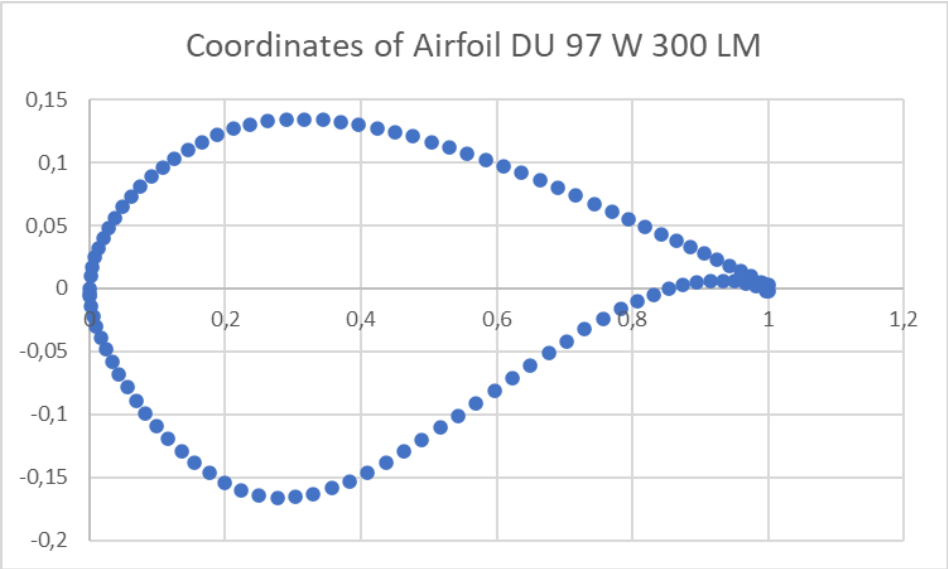

Figure 3.1.3 DU 97 W 300 LM

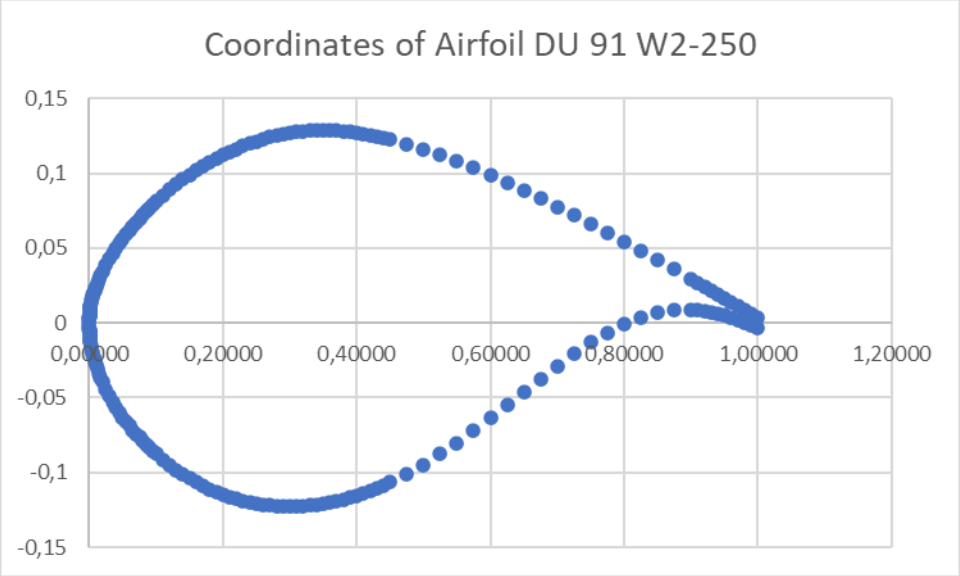

Figure 3.1.4 DU 91 W2-250

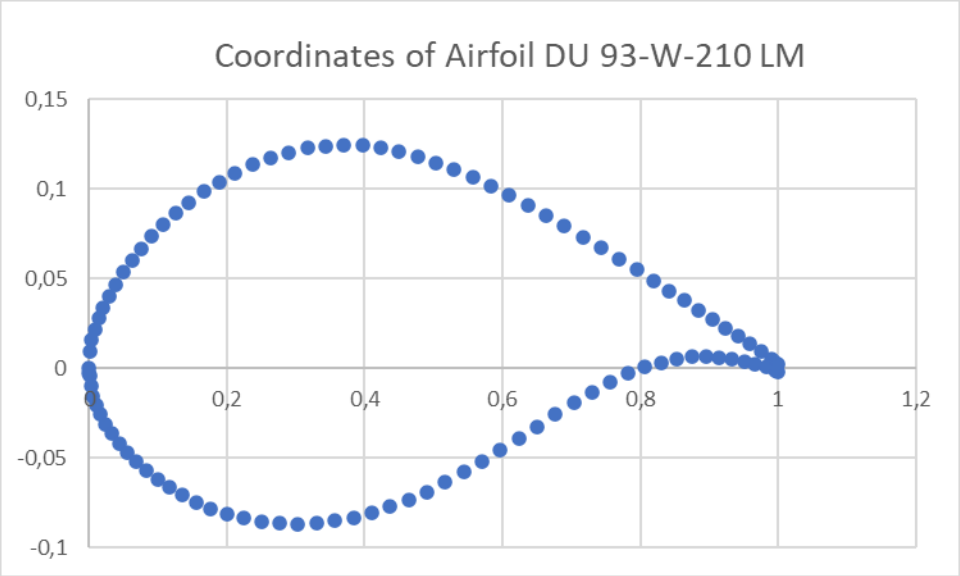

Figure 3.1.5 DU 93-W-210 LM

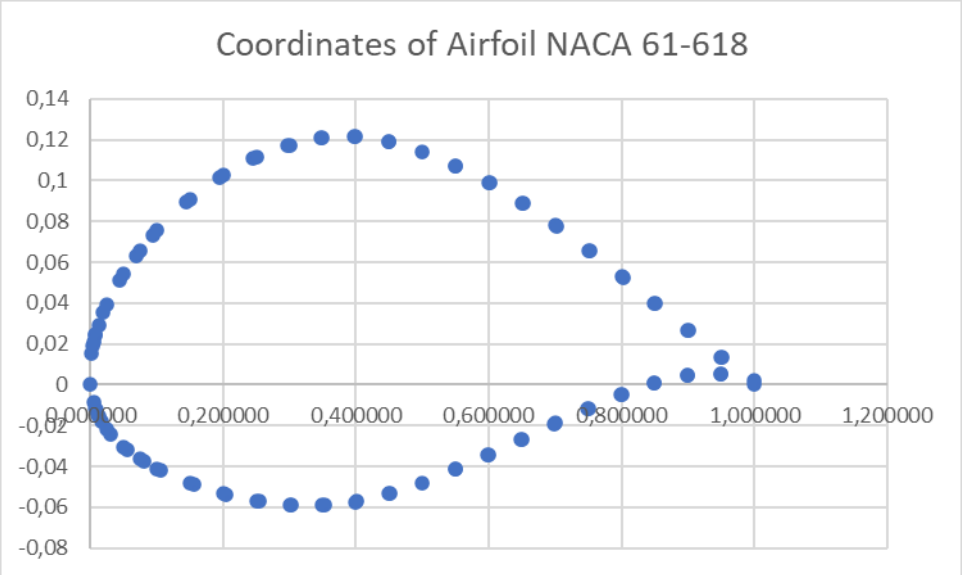

Figure 3.1.6 NACA 61-618

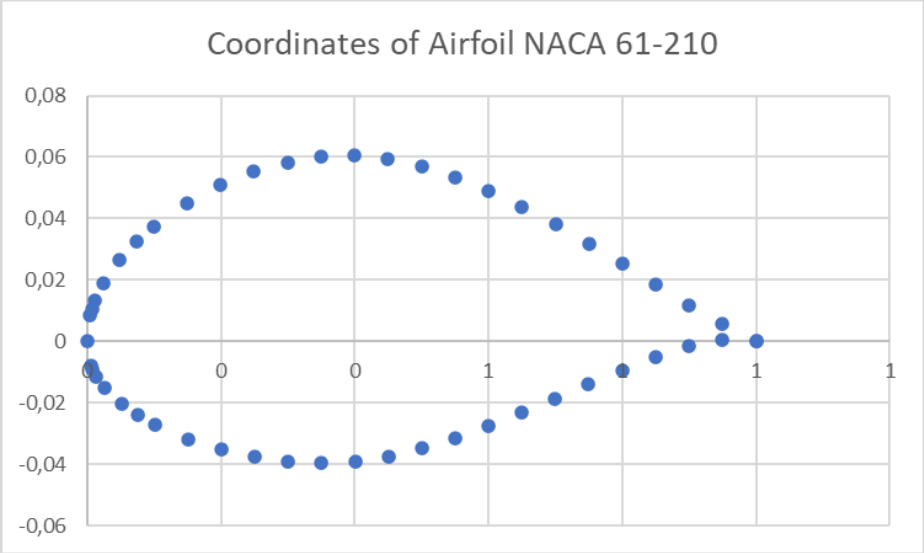

Figure 3.1.7 NACA 61-210

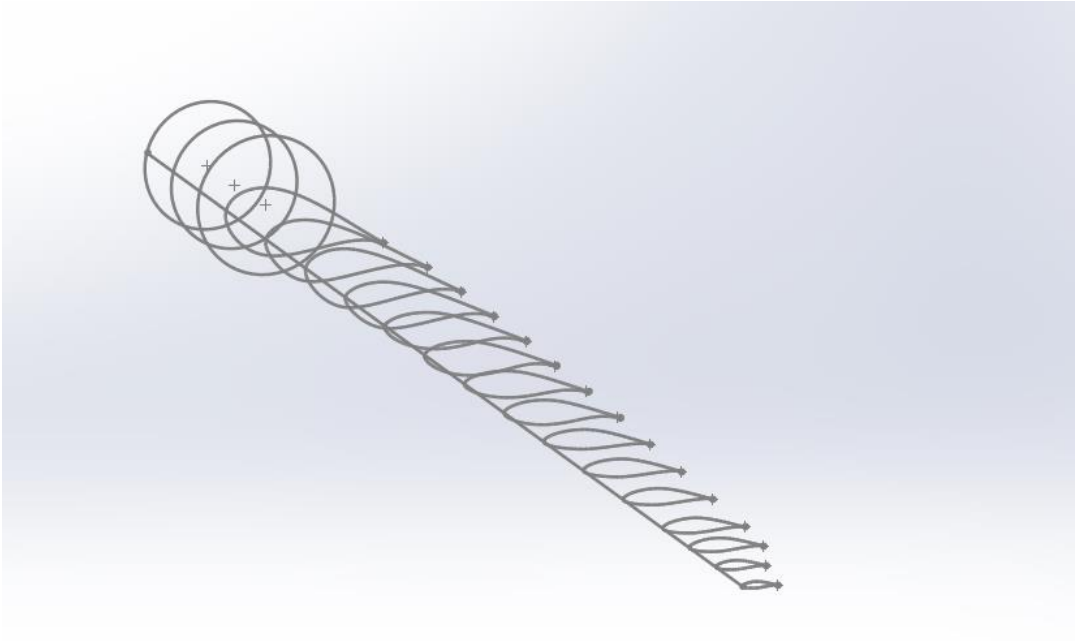

Figure 3.1.8 CAD of the unmodified airfoil

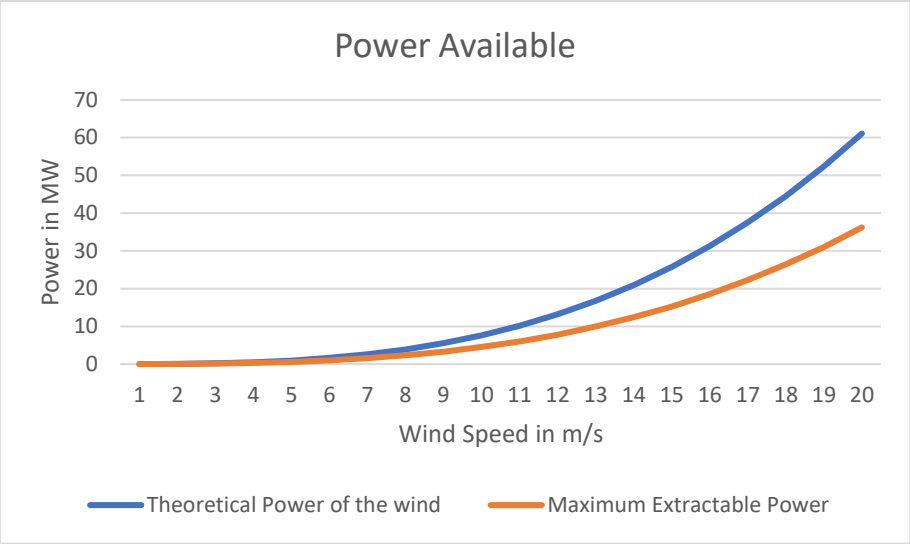

Figure 3.1.9 Maximum extractable power depending on wind speed.

Table 3.1.2 Modified Rotor

Node	Rnodes (m)	r/R	AeroTwist Theta T(º)	DRNodes (m)	Chord Length(m)	Airfoil Type
1	2.8667	0.0455	13.308	2.7333	3.542	Cylinder 1
2	5.6000	0.0888	13.308	2.7333	3.854	Cylinder 1
3	8.3333	0.1322	13.308	2.7333	4.167	Cylinder 2
4	11.7500	0.1865	13.308	4.1000	4.557	DU 99 W 405 LM
5	15.8500	0.2515	11.480	4.1000	4.652	DU 99 W 350
6	19.9500	0.3166	10.162	4.1000	4.458	DU 99 W 350
7	24.0500	0.3817	9.560	4.1000	4.249	DU 97 W 300 LM
8	28.1500	0.4468	7.795	4.1000	4.007	DU 91 W2-250
9	32.2500	0.5119	6.544	4.1000	3.748	DU 91 W2-250
10	36.3500	0.5769	5.361	4.1000	3.502	DU 93-W-210 LM
11	40.4500	0.6420	4.188	4.1000	3.256	DU 93-W-210 LM
12	44.5500	0.7071	3.125	4.1000	3.050	DU 93-W-210 LM
13	48.6500	0.7722	2.319	4.1000	2.764	NACA 64-618
14	52.7500	0.8373	1.526	4.1000	2.518	NACA 64-618
15	56.1667	0.8915	0.863	2.7333	2.313	NACA 64-618
16	58.9000	0.9349	0.350	2.7333	2.055	NACA 64-210
17	61.6333	0.9783	0.015	2.7333	1.850	NACA 64-210

3.2 Analysis of the rotor at rated wind speed

The rotor is studied applying the blade element momentum theory. Therefore, the rotor is divided into the sections established in the table above. Once the sections are established the iterative process of the BEM theory method starts. Starting at the most inboard segment of the blade, setting the axial and angular induction factors to zero. With the assumption of both induction factors being equal to zero, the angle of the resultant velocity is calculated using Eq. 3.2.1

$$\varphi = \tan^{-1}\left(\frac{V_\infty(1-a)}{\Omega r(1+a')}\right) \quad \text{(Eq 3.2.1)}$$

Knowing the local angle of the resultant velocity, the local angle of attack is calculated using Eq. 3.2.2.

$$\alpha = \varphi - (\theta_{CP} + \theta_T) \quad \text{(Eq 3.2.2)}$$

The lift and drag coefficients can be computed as they are a function of the local angle of attack. The coefficients for Eq. 3.2.3 and Eq. 3.2.4 for lift and drag respectively are a property given by the geometry of the airfoil. These coefficients for lift and drag are listed in Table 3.2.1. and Table 3.2.2 respectively. For the cylinders, the lift and drag coefficients can be determined due to the ease of their shape. These are specified in Table 3.2.3.

$$C_l = C_{l1} + C_{l2}\alpha + C_{l3}\alpha^2 + C_{l4}\alpha^3 + C_{l5}\alpha^4 \quad \text{(Eq 3.2.3)}$$

$$C_d = C_{d1} + C_{d2}\alpha + C_{d3}\alpha^2 + C_{d4}\alpha^3 + C_{d5}\alpha^4 \quad \text{(Eq 3.2.4)}$$

Table 3.2.1

	C_1	C_2	C_3	C_4	C_5
DU 99 W 405 LM	0.19393324	0.11219533	5.86E-03	-7.09E-04	1.65E-05
DU 99 W 350	1.90E-01	1.11E-01	1.09E-02	-1.16E-03	2.56E-05
DU 97 W 300 LM	2.82E-01	1.48E-01	9.28E-04	-6.40E-04	1.77E-05
DU 91 W2-250	4.81E-01	1.48E-01	-6.41E-03	-4.20E-05	4.61E-06
DU 93-W-210 LM	5.66E-01	1.31E-01	-5.58E-03	-3.99E-05	3.81E-06
NACA 64-618	-5.09E-02	3.01E-02	1.44E-02	1.07E-03	-1.81E-04
NACA 64-210	-4.63E-02	2.74E-02	1.31E-02	9.74E-04	-1.65E-04

Table 3.2.2

	C_1	C_2	C_3	C_4	C_5
DU 99 W 405 LM	2.09E-02	-2.73E-03	-9.16E-04	1.87E-04	-4.34E-06
DU 99 W 350	1.01E-02	1.11E-02	-3.70E-03	3.24E-04	-6.50E-06
DU 97 W 300 LM	1.33E-02	1.82E-03	-1.60E-03	1.95E-04	-4.37E-06
DU 91 W2-250	7.23E-03	-1.07E-03	-1.93E-04	7.56E-05	-1.74E-06
DU 93-W-210 LM	6.97E-03	-6.92E-04	-1.47E-04	5.54E-05	-1.10E-06
NACA 64-618	-2.02E-03	2.70E-02	-6.17E-03	4.85E-04	-6.18E-06
NACA 64-210	-2.23E-03	2.98E-02	-6.81E-03	5.35E-04	-6.82E-06

Table 3.2.3

	C_L	C_D
Cylinder 1	0	0.5
Cylinder 2	0	0.35

With the values of the lift and drag coefficients for normal and tangential force are introduced using Eq. 3.2.5 and Eq. 3.2.6 respectively.

$$C_N = C_L \cos\varphi + C_D \sin\varphi \quad \text{(Eq 3.2.5)}$$

$$C_T = C_L \sin\varphi - C_D \cos\varphi \quad \text{(Eq 3.2.6)}$$

To simply the calculation processes the parameter σ_r is introduced as Eq. 3.2.7

$$\sigma_r = \frac{Bc}{2\pi r} \quad \text{(Eq 3.2.7)}$$

The new values of *a* and *a'* are calculated using Eq. 3.2.8 and 3.2.9 and compared to the value calculated in the previous iteration. If both fulfill the condition of $\Delta < 0.0001$ the value is considered acceptable, the torque *Q* Eq. 3.2.9, the thrust *T* Eq. 3.2.10, and the power *P* Eq. 3.2.11 on that segment can be calculated and the process repeated for the next segment.

$$a = \frac{1}{\frac{4\,(\sin\varphi)^2}{\sigma_r C_N} + 1} \quad \text{(Eq 3.2.8)}$$

$$a' = \frac{1}{\frac{4\sin\varphi\cos\varphi}{\sigma_r C_T} - 1} \quad \text{(Eq 3.2.9)}$$

$$dQ = 0.5B\rho v_r^2 C_T c r dr \quad \text{(Eq 3.2.10)}$$

$$dT = 2\rho v_\infty^2 a(1-a)2\pi r dr \quad \text{(Eq 3.2.11)}$$

$$dP = \Omega \mathrm{dQ} \quad \text{(Eq 3.2.12)}$$

To compensate for losses due to pressure differences that change the flow around the airfoil, the Prandtl tip loss factor *F'* is introduced to account for this phenomenon. Empirical evidence suggests that for a radial segment in relation to the radius below 0,6 this factor is approximately 1 and is therefore negligible. This claim can be determined to be certain observing the value of *F'* at rotor segment 10, located at relative radius of 0,57 being 0,9984. Above 0.6 however this factor is defined as Eq. 3.2.13. The values of *F'* as a function of *r/R* is plotted in figure 3.2.1.

$$F' = \frac{2}{\pi} \times \sin^{-1}(e^{-f}) \quad \text{(Eq 3.2.13)}$$

Being *f* a factor depending on the number of blades, the radius, the radial position and the angle the resultant velocity creates with the plane of rotation once the rotor starts spinning, calculated in Eq. 3.2.14.

$$f = \frac{B}{2} \times \frac{R - r}{r \times \sin \varphi} \qquad \text{(Eq 3.2.14)}$$

The correction factors for the BEM theory proposed derived by Glauert to compensate for flow entrance from outside of the wake is negligible for induction factors smaller than 0,4. After the iterative calculation process it is determined that there is no point over the entire rotor that surpasses this limit.

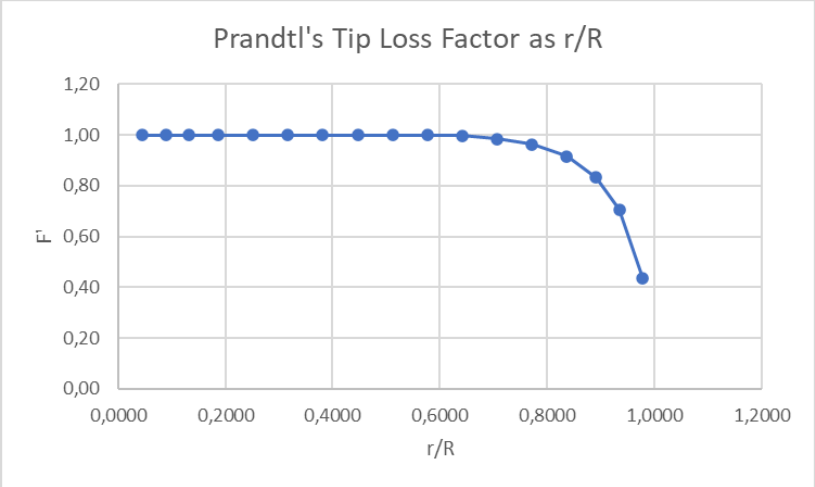

Figure 4.2.1 F as a function of r/R

The detailed results for each of the key variables of applying this process for every segment at the minimum wind speed that, under design conditions, which is with a value for lambda of 7, reaches maximum possible power output, nine megawatts, are displayed in Appendix. The evolution of power, the axial induction factor as well as the local angle of attack are plotted as a function of *r/R* in figures 3.2.2, 3.2.3 and 3.2.4.

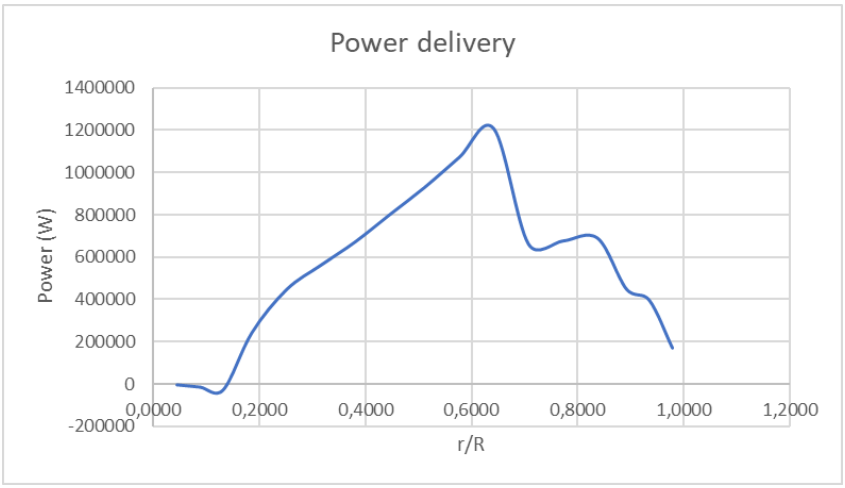

Figure 3.2.2 Power delivery as function of r/R

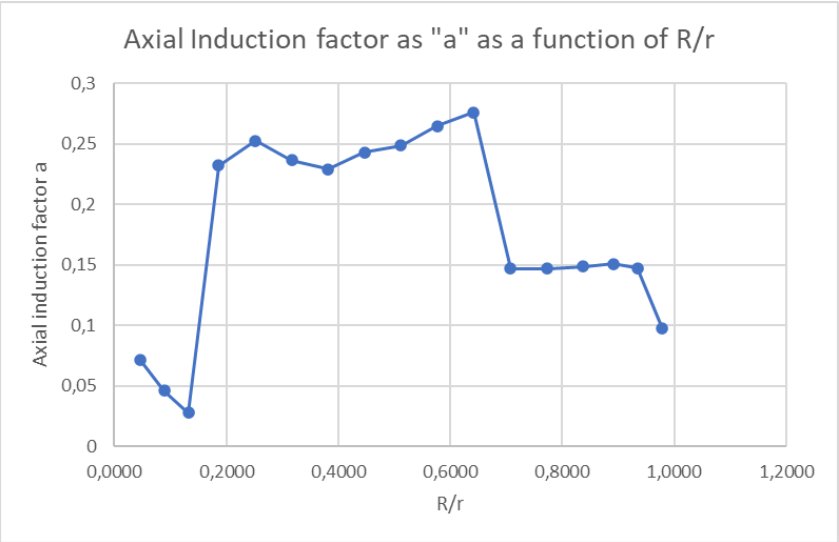

Figure 3.2.3 Axial induction factor as a function of r/R

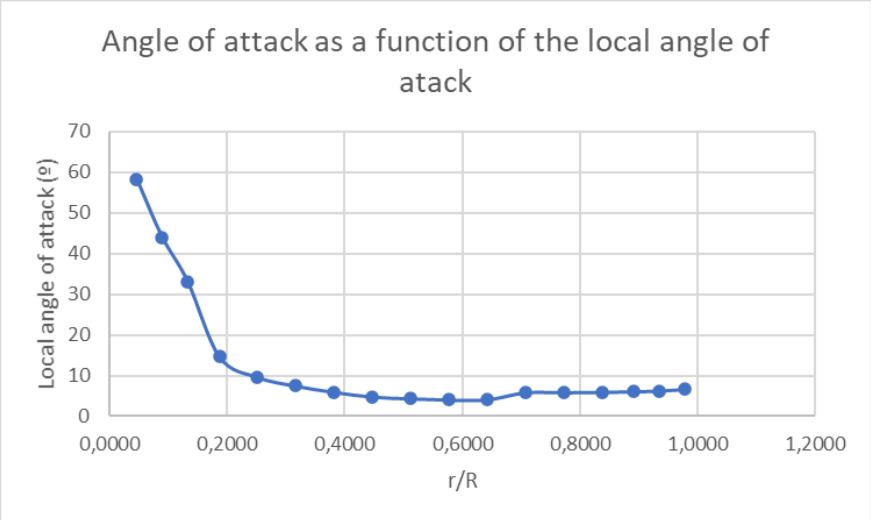

Figure 3.2.4 Local angle of attack as a function of r/R

3.3 Wake Generation of this rotor

Wake is the denomination of the turbulent stream that is created by the wind turbine extracting energy from the wind. This stream opens in a cone that is tangent to the disk the rotor symbolizes. It requires a certain distance downstream of the rotor for the wind to get back to ambient velocity. The wake strongly depends on the axial induction factor, which is another reason why in farms it is key to operate close to the Betz limit. Under normal operating conditions the wake generation of this rotor is developed in this section. Given the values of Figure 3.2.4 of the axial induction, it is fair to use and overall value of $a = 0.25$ for these calculations. The constant that defines the evolution of speed deficit along the wake is given by Eq. 3.3.1

$$\gamma = \frac{0.5}{\ln \frac{z}{z'}} = \frac{0.5}{\ln \frac{120}{0.0002}} = 0.04 \qquad \text{(Eq 3.4.1)}$$

The other value that describes is the so-called downstream rotor radius, this is a virtual radius that characterizes the wake width. This is given in Eq. 3.3.2.

$$r_d = R\sqrt{\frac{1 - a}{1 - 2a}} = 77.16 \quad \text{(Eq 3.3.2)}$$

With both characteristic values of the wake, the deficit as a function of the distance to the physical rotor is given by Eq. 3.3.3.

$$v_d = \frac{2a}{1 + \gamma(\frac{x}{r_d})^2} \quad \text{(Eq 3.3.3)}$$

Therefore, the velocity at a certain point within the wake regarding the ambient speed is given by Eq. 3.3.4.

$$v_W = v_\infty(1 - v_d) \quad \text{(Eq 3.3.4)}$$

Iterating that process for several distances leads to the results plotted in Figure 3.3.1.

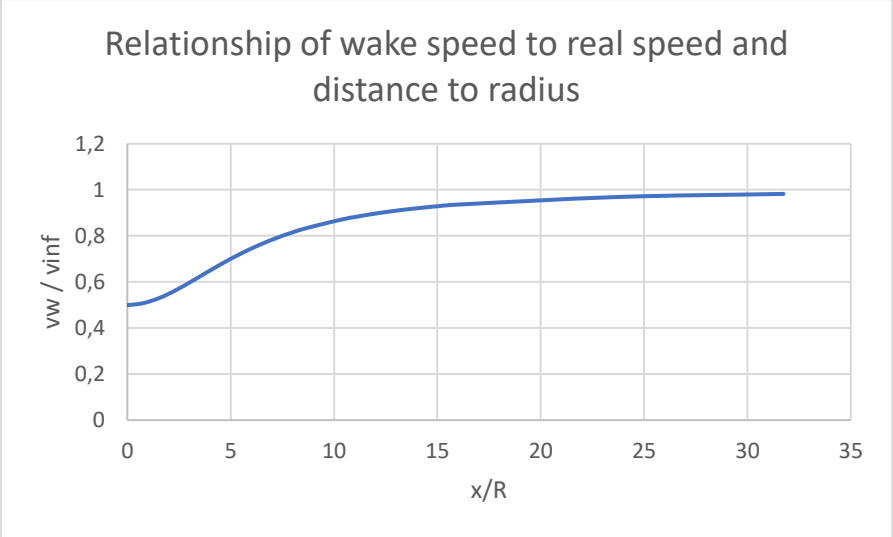

Figure 3.3.1 Evolution of wake speed to ambient speed as a function of distance to radius

3.4 Analysis of the rotor at worst case scenario.

In this part the structural response of each individual rotor blade in different load scenarios is calculated, first mathematically and then backed up with simulations of a finite element method to verify the results. The worst scenario of highest loading condition is determined by comparing the evolution of thrust and torque as a function of the wind speed for the design value of lambda, the results are plotted in figure 3.4.2 and shows that the critical point is the initial point of the rated power area, as for after that the power output is kept constant, but the rotational speed keeps increasing, therefore the load state can decrease. Considering two potential control methods, which are, changing the pitch of the rotor blades or changing the tip-speed ratio, which alters the rotational speed Ω of the rotor. The alteration of the tip-speed ratio will inevitably cause a loss of

aerodynamic efficiency taking the value of the axial induction factor *a* further away from the ideal value determined by the Betz limit, one third, however it offers the possibility of sacrificing efficiency for reducing thrust and torque by allowing shallower angles of attack. This is demonstrated in Figures 3.4.3, 3.4.4, 3.4.5, and 3.4.6 comparing normal and tangential force as well as thrust and torque for values above and below the design value of lambda, 7. Therefore, the load which is used for the structural analysis of the rotor and the input loads onto the main shaft, will be a combination of all possible worst states' times the correspondent security factor as represented in Figure 3.4.1.

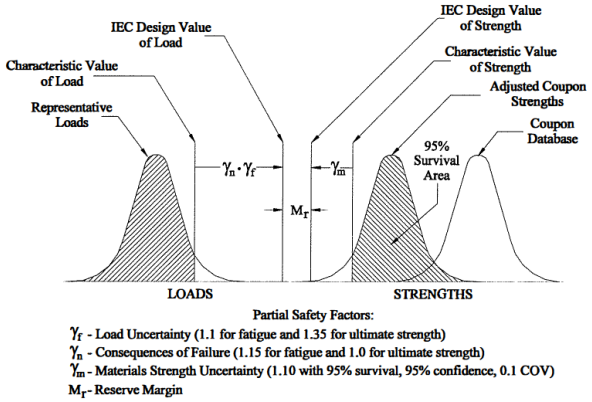

Figure 3.4.1 Safety Factors [5]

Criteria of minimum thickness of the turbine blade. Determining the absolute highest statistical load measured with the security coefficient of three times ten percent variation leads to Eq. 3.4.1

$$v_{sec} = (24.75 + 3 \times 2.475)\frac{\ln((120)/0.0002)}{\ln(0.5/0.0002)} = 53.94\ m/s \qquad \text{(Eq 3.4.1)}$$

The aerodynamic load is the calculated with Eq. 3.4.2 with lift coefficient assumed to be constant over the entire blade and set at a value of 1.5, the chord length being the average, 3.4 meters and the density of the air to be 1.25.

$$L = 0.5 \times 1.25 \times 53.94^2 \times 1.5 \times 3.4 = 9974\ N/m \qquad \text{(Eq 3.4.2)}$$

The bending moment is then given by Eq. 3.4.3, assuming that the load calculated with 3.4.2 is present over the entire length of the span.

$$M = \int_1^{63} rL(r)dr\ = 19\ 788\ 416\ Nm \qquad \text{(Eq 3.4.3)}$$

The minimum thickness is consequently given by Eq. 3.4.4 knowing that W = 0.56

$$T_{min} = \frac{19\ 788\ 416}{0.56 \times 0.48 \times (4/3) \times 3300000000} = 0.016\ m \qquad \text{(Eq 3.4.4)}$$

3.5 Analysis of the blade under standard conditions

For proper choice of standard operations loads different loading scenarios are developed in Figures 3.5.1, 3.5.2, 3.5.3, 3.5.4, and 3.5.5.

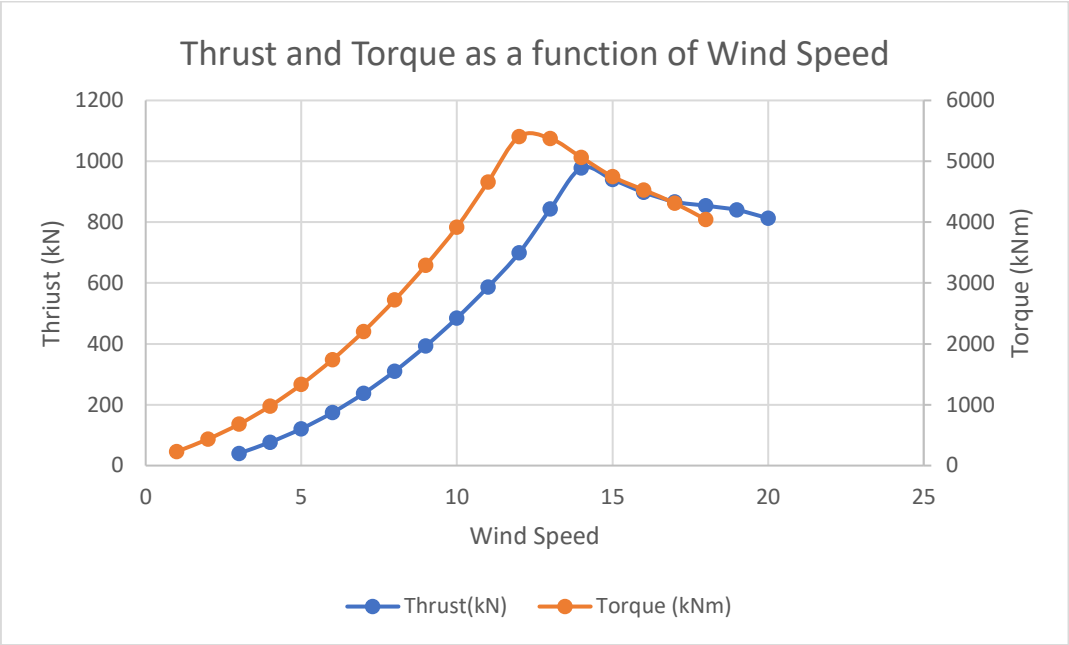

Figure 3.5.1 Thrust and Torque as a function of wind speed at lambda = 7

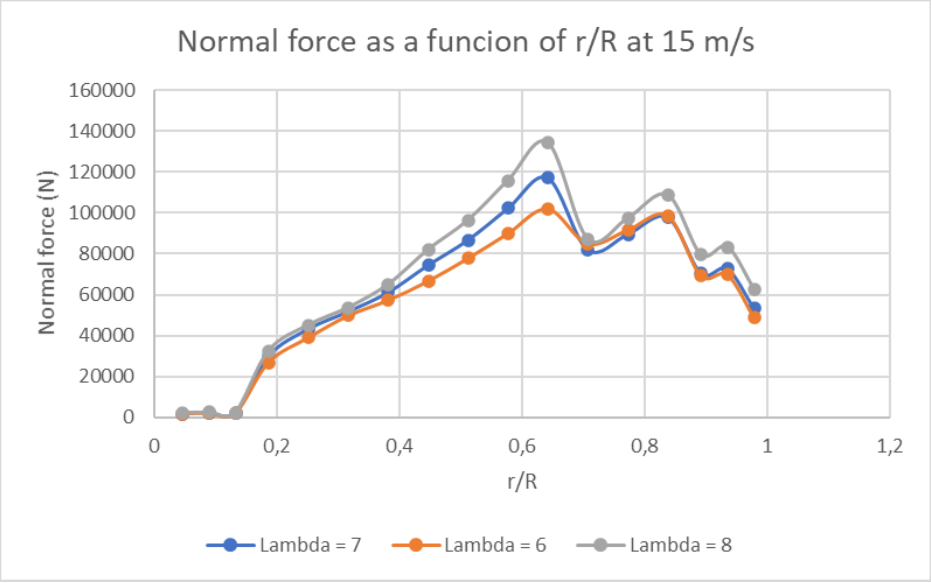

Figure 3.5.2 Normal force as a function of r/R and lambda

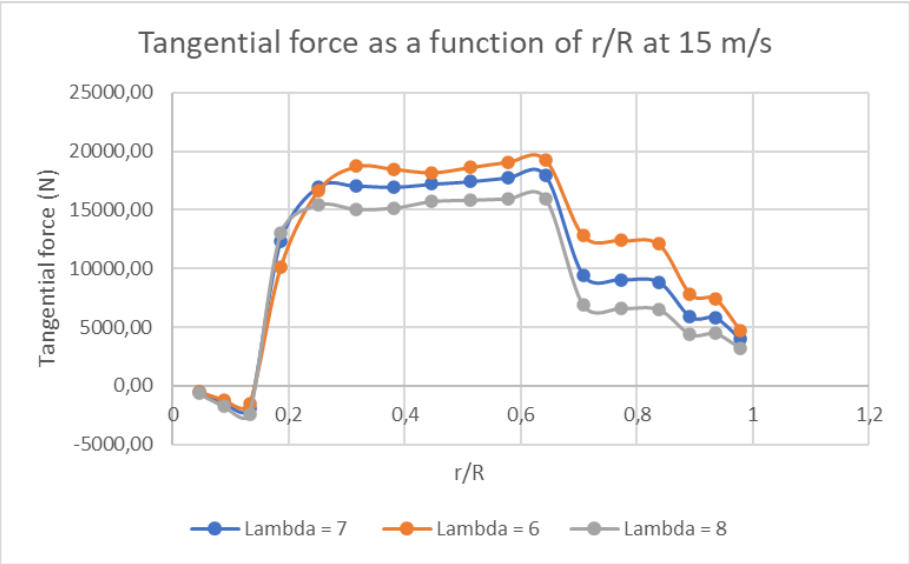

Figure 3.5.3 Tangential force as a function of r/R and lambda

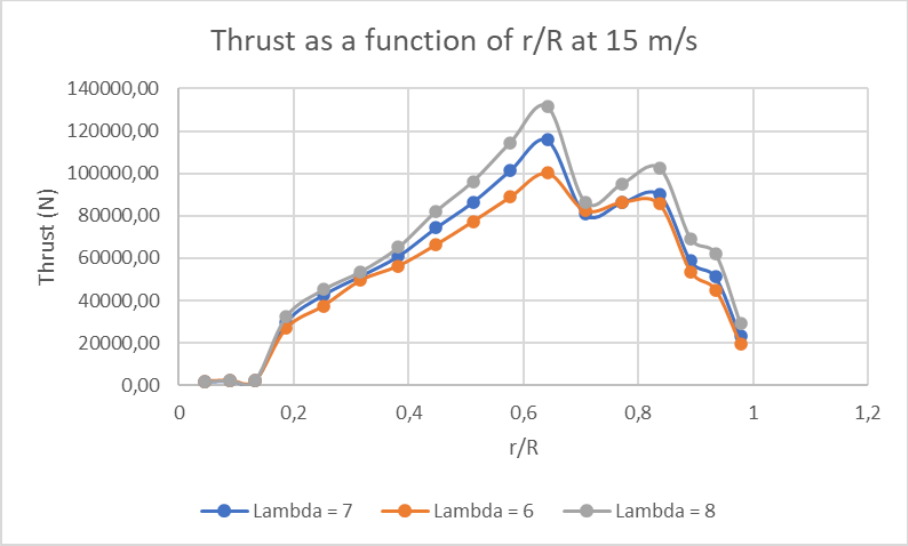

Figure 3.5.4 Thrust as a function of r/R and lambda.

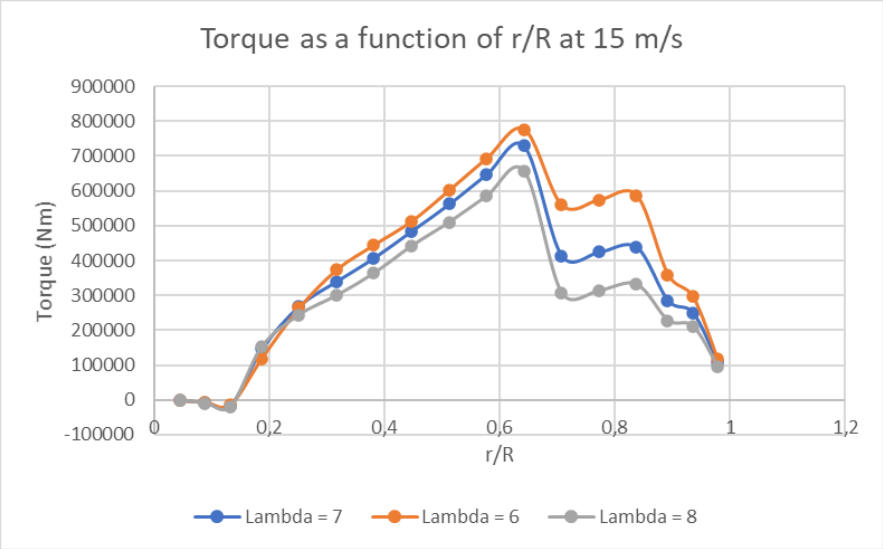

Figure 3.5.5 Torque as a function of r/R and lambda.

After comparing all the previously developed situation the load case that puts the highest stress on the blade is determined to be with the lowest lambda at rated speed. To conduct a bidimensional analysis of deflection, initially the inertia of the principal axis and the angle to local axis is determined using computational tools. The values for each section are described in table 3.5.1.

Table 3.5.1 Main axis inertias and their respective angle

Node	Iz (m4)	Iy (m4)	Angle with local chord line (º)
1	7,73E+00	7,73E+00	0
2	7,73E+00	7,73E+00	0
3	1,08E+01	1,08E+01	0
4	4,77E+00	9,40E-01	2,64
5	4,42E+00	6,90E-01	2,91
6	3,73E+00	5,80E-01	2,91
7	2,46E+00	2,70E-01	2,94
8	1,63E+00	1,50E-01	2,63
9	1,25E+00	1,20E-01	2,62
10	8,70E-01	5,00E-02	1,73
11	6,50E-01	3,00E-02	1,73
12	4,40E-01	2,00E-02	0,76
13	3,10E-01	1,00E-02	0,76
14	2,10E-01	1,00E-02	0,76
15	1,50E-01	1,00E-02	0,76
16	1,00E-01	4,00E-03	0,76
17	1,40E-01	6,00E-03	0,72

Using the discretized segments of blade to compute the loads leaves them as a function of the load distribution of each segment, *N/m*, p_z and p_y can be determined by equally distributing the tangential and normal force on each blade and dividing it by the respective radial difference which is equal to *dr*. The resultant values are shown in table 3.5.2.

Table 3.5.2 Load per meter for each blade segment

Forces on the Blade	pz (N/m)	Py (N/m)
Segment 1	2,10E+02	-6,70E+01
Segment 2	2,85E+02	-1,77E+02
Segment 3	2,59E+02	-2,40E+02
Segment 4	2,90E+03	1,22E+03
Segment 5	3,48E+03	1,38E+03
Segment 6	4,16E+03	1,38E+03
Segment 7	4,91E+03	1,37E+03
Segment 8	5,99E+03	1,39E+03
Segment 9	6,97E+03	1,41E+03
Segment 10	8,22E+03	1,44E+03
Segment 11	9,43E+03	1,45E+03
Segment 12	6,45E+03	7,37E+02
Segment 13	7,04E+03	7,06E+02
Segment 14	7,70E+03	6,89E+02
Segment 15	6,65E+03	5,48E+02
Segment 16	8,57E+03	6,75E+02
Segment 17	6,28E+03	4,61E+02

The differential summation to determine the shear stress can than be done setting the boundary condition to be that the shear stress at the outboard segment is null. In table 3.5.3 the resultant shear stress is then.

Table 3.5.3 Resultant Shear Stress

Forces on the Blade	Tz (N)	Ty (N)
Segment 1	3,26E+05	5,62E+04
Segment 2	3,26E+05	5,65E+04
Segment 3	3,25E+05	5,71E+04
Segment 4	3,20E+05	5,54E+04
Segment 5	3,07E+05	5,01E+04
Segment 6	2,91E+05	4,44E+04
Segment 7	2,72E+05	3,88E+04
Segment 8	2,50E+05	3,31E+04
Segment 9	2,23E+05	2,74E+04
Segment 10	1,92E+05	2,16E+04
Segment 11	1,56E+05	1,56E+04
Segment 12	1,23E+05	1,12E+04
Segment 13	9,58E+04	8,20E+03
Segment 14	6,56E+04	5,34E+03
Segment 15	4,11E+04	3,22E+03
Segment 16	2,03E+04	1,55E+03
Segment 17	0,00E+00	0,00E+00

Applying than the differential summation for the bending moments knowing the shear stress and the elements of force along the segment leads to the results shown in Table 3.5.4. Once known the bending moments along the reference axis, these must be transposed into the principal axis of each segment, this needs to consider the twist angle of each segment θ_T and the angle of the principal axis of inertia of each segment to the reference axis, β.

Table 3.5.4 Bending moments

Forces on the Blade	Mz (Nm)	My (Nm)	M1 (Nm)	M2 (Nm)
Segment 1	-1,68E+06	-1,18E+07	-1,11E+07	-1,09E+06
Segment 2	-1,52E+06	-1,09E+07	-1,03E+07	-1,03E+06
Segment 3	-1,37E+06	-1,00E+07	-9,44E+06	-9,78E+05
Segment 4	-1,17E+06	-8,92E+06	-8,26E+06	-1,32E+06
Segment 5	-9,57E+05	-7,64E+06	-7,16E+06	-9,71E+05
Segment 6	-7,63E+05	-6,41E+06	-6,07E+06	-7,07E+05
Segment 7	-5,93E+05	-5,26E+06	-5,02E+06	-5,09E+05
Segment 8	-4,45E+05	-4,18E+06	-4,04E+06	-3,19E+05
Segment 9	-3,21E+05	-3,21E+06	-3,12E+06	-1,95E+05
Segment 10	-2,21E+05	-2,36E+06	-2,31E+06	-7,23E+04
Segment 11	-1,44E+05	-1,64E+06	-1,62E+06	-2,59E+04
Segment 12	-9,04E+04	-1,07E+06	-1,07E+06	1,74E+04
Segment 13	-5,08E+04	-6,24E+05	-6,21E+05	1,72E+04
Segment 14	-2,31E+04	-2,93E+05	-2,91E+05	1,14E+04
Segment 15	-8,59E+03	-1,11E+05	-1,11E+05	5,44E+03
Segment 16	-1,99E+03	-2,63E+04	-2,63E+04	1,47E+03
Segment 17	0	0	0,00E+00	0,00E+00

With the bending moments transposed to the principal axis and knowing the inertia along these axes for each segment from Table 3.5.1, the curvature the bending causes along the main axes can be determined. These curvatures are than again transposed back into the global reference system and are presented in Table 3.5.5.

Table 3.5.5 Curvatures

Forces on the Blade	k1(1/m)	k2(1/m)	Kz (1/m)	Ky (1/m)
Segment 1	-1,69E-04	-1,65E-05	2,28E-05	-1,68E-04
Segment 2	-1,56E-04	-1,57E-05	2,07E-05	-1,56E-04
Segment 3	-1,03E-04	-1,06E-05	1,33E-05	-1,02E-04
Segment 4	-2,04E-04	-1,66E-04	-1,03E-04	-2,41E-04
Segment 5	-1,91E-04	-1,66E-04	-1,13E-04	-2,26E-04
Segment 6	-1,92E-04	-1,43E-04	-9,63E-05	-2,19E-04
Segment 7	-2,40E-04	-2,22E-04	-1,67E-04	-2,81E-04
Segment 8	-2,91E-04	-2,50E-04	-1,94E-04	-3,32E-04
Segment 9	-2,94E-04	-1,91E-04	-1,42E-04	-3,20E-04
Segment 10	-3,13E-04	-1,70E-04	-1,30E-04	-3,32E-04
Segment 11	-2,93E-04	-1,02E-04	-7,08E-05	-3,02E-04
Segment 12	-2,85E-04	1,02E-04	1,21E-04	-2,78E-04
Segment 13	-2,36E-04	2,02E-04	2,15E-04	-2,24E-04
Segment 14	-1,63E-04	1,34E-04	1,40E-04	-1,58E-04
Segment 15	-8,71E-05	6,40E-05	6,64E-05	-8,53E-05
Segment 16	-3,09E-05	4,32E-05	4,38E-05	-3,00E-05
Segment 17	0,00E+00	0,00E+00	0,00E+00	0,00E+00

These values are then used to discretized calculations of the angle of deformation, being the support end of the blade rigid, there boundary condition is set that the deformation along both axes at the beginning is null. Iterating this process leads to the results shown in table 3.5.6

Table 3.5.6 Angles of deformation

Forces on the Blade	Thz	Thy
Segment 1	0	0
Segment 2	5,95E-05	-4,43E-04
Segment 3	1,06E-04	-7,96E-04
Segment 4	-4,78E-05	-1,38E-03
Segment 5	-4,91E-04	-2,34E-03
Segment 6	-9,20E-04	-3,25E-03
Segment 7	-1,46E-03	-4,28E-03
Segment 8	-2,20E-03	-5,53E-03
Segment 9	-2,89E-03	-6,87E-03
Segment 10	-3,44E-03	-8,21E-03
Segment 11	-3,86E-03	-9,50E-03
Segment 12	-3,75E-03	-1,07E-02
Segment 13	-3,06E-03	-1,17E-02
Segment 14	-2,34E-03	-1,25E-02
Segment 15	-1,98E-03	-1,29E-02
Segment 16	-1,83E-03	-1,31E-02
Segment 17	-1,77E-03	-1,31E-02

Finally, the local curvature and bending angles are used to discretize the local displacement value along the global reference axes the deformation is shown in Table 3.5.7 and figure 3.5.7.

Table 3.5.7 Displacements

Forces on the Blade	uz (m)	uy (m)
Segment 1	0	0
Segment 2	-6,13E-04	8,26E-05
Segment 3	-2,34E-03	3,13E-04
Segment 4	-5,92E-03	5,26E-04
Segment 5	-1,36E-02	-5,65E-04
Segment 6	-2,51E-02	-3,48E-03
Segment 7	-4,04E-02	-8,26E-03
Segment 8	-6,04E-02	-1,57E-02
Segment 9	-8,59E-02	-2,62E-02
Segment 10	-1,17E-01	-3,92E-02
Segment 11	-1,53E-01	-5,43E-02
Segment 12	-1,95E-01	-7,01E-02
Segment 13	-2,41E-01	-8,42E-02
Segment 14	-2,90E-01	-9,52E-02
Segment 15	-3,34E-01	-1,03E-01
Segment 16	-3,69E-01	-1,08E-01
Segment 17	-4,05E-01	-1,13E-01

As it can be seen in the table the values for the displacement along the y axis is in relationship to the scale of the construction so small that it can be negligible. The displacement along the z axis however needs to be considered for further design measures to avoid incidents like collisions with the tower. Furthermore, a finite element analysis is conducted with the blade to determine the accuracy of the discretized values, equally setting the boundary conditions to the outer nodes be fixed and loading the blade with p as N/m. The results of this analysis show the resultant stress on the blade in Figure 3.5.8 and the displacement in Figure 3.5.7. As mentioned previously in the part of the blade geometry, the tip shape has been changed to reduce the deflection, result shown in Figure 3.5.6. Comparing Figure 3.5.6 and 3.5.5 it shows that not only is the overall deflection is minor, but also the curvature and increase of the deflection towards the tip is more uniform. These simulations have been conducted under the following boundary conditions; the end that connects to the hub is fixed, i.e. no displacement and no misalignment allowed and the blade is receiving aerodynamic load at 25 m/s at pitch angle 0^{o}.

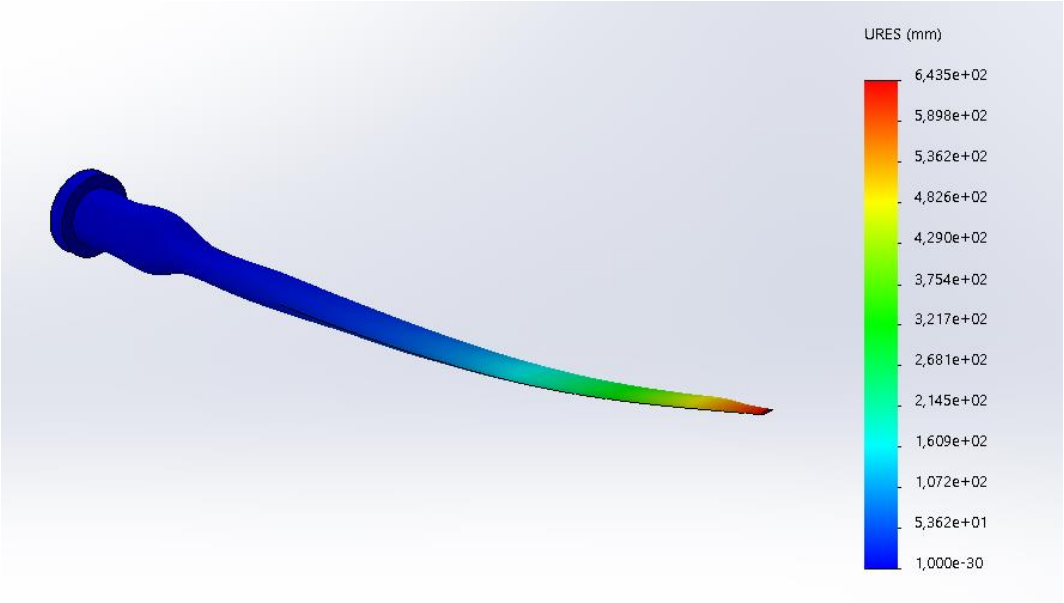

Figure 3.5.6 Deflection with the original tip shape

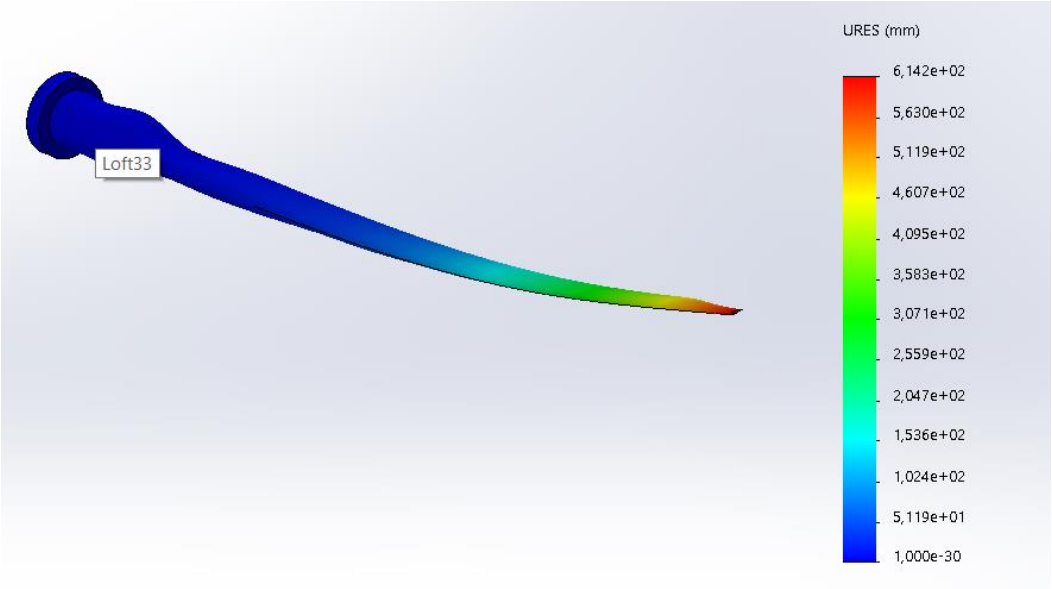

Figure 3.5.7 Deflection with the modified tip shape

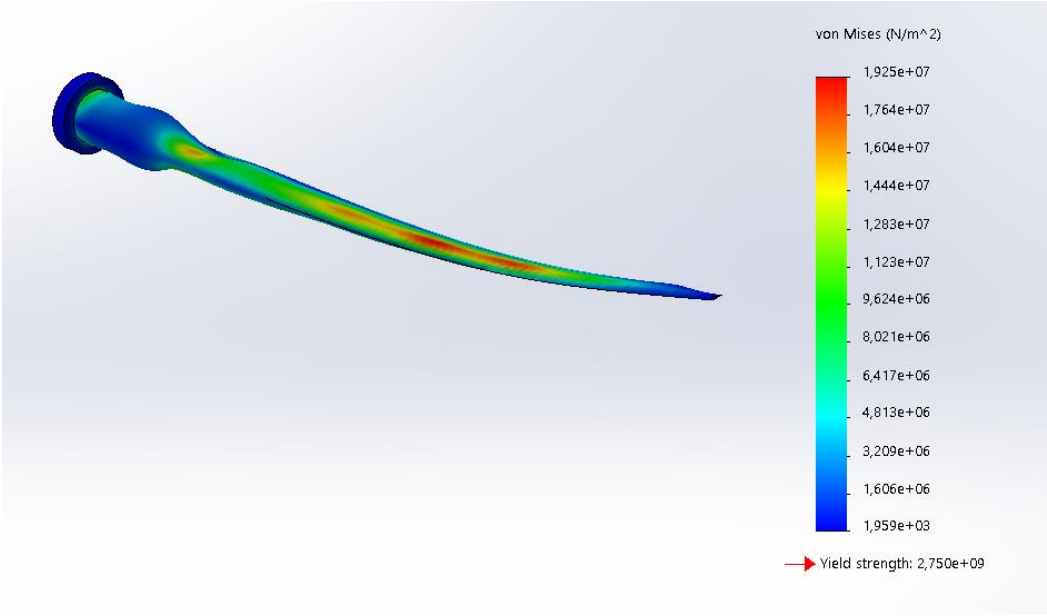

Figure 3.5.8 von Mises stress along the blade

From this it can be concluded that the resultant stress according to Van Mises is significantly smaller than the stress applied. The displacement calculated with this method however is higher than the one realized in the previous manual calculations. This new value will be the critical design value.

4 Design of the drive train

Once having calculated the maximum load state the mechanical complex is submitted to the design of it begins. For wind turbines in this magnitude order there are two main approaches on how to convert the mechanical into electrical energy. The first of these approaches is employing a classical mechanical transmission, a.k.a. a gear box to augment the approximately sixteen revolutions per minute the low-speed shaft is spinning at to fifteen hundred revolutions per minute that are used as input to the high-speed electrical generator. The second approach is to employ a direct drive system that connects the input shaft to a synchronous permanent magnet system. To decide which of the two systems is to be preferred a trade study is conducted.

4.1 Trade Study

To compare whether a direct drive or a gearbox system should be employed to transform the mechanical into electrical energy, focus is set on two key aspects: reliability and efficiency. The power capability does not really restrict any of both systems, however, in the case of the gearbox translates into a higher amount of reductions stages which, at the time, is equivalent to a reduction of the overall reliability of the system. Figure 4.1.1 [7] shows the percentage made up on failure and on costs, on average of the different elements of a wind turbine.

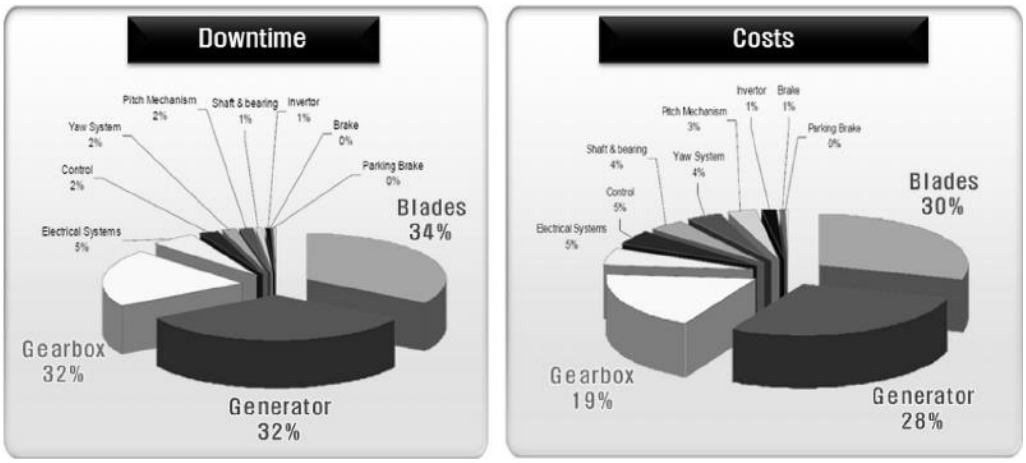

Figure 4.1.1 Reliability and Cost of Wind Turbine Components [7]

As shown in Figure 4.1.1 it becomes clear that a Gearbox makes up a third of the total downtime of a wind turbine and occupies a fifth of the cost of manufacturing. It is obvious that in direct drive systems, the cost of the generator is higher than the one in a conventional transmission, it reduces however drastically the probability of failure, reduces maintenance cost, and allows a bit more of a flexible operation of the turbine for it is not as limited by the input rotational speed as conventional generators. It is therefore that a direct drive system is preferred to be installed.

4.2 Main Shaft

Having the determined the stresses that the rotor transmits onto the low-speed shaft, the design process of it can begin. It is composed out of three major areas; area one is the plate the hub is bolted onto, area two contains the bearings which connect the shaft to the bed plate, area three is the coupling between the shaft and the generator. Making use of Kisssoft and the bearing selecting tool of SKF the shaft is dimensioned and the bearing

are sized. After a brief stress and bearing life analysis it becomes very clear that the major concerns are the lubrication and thermal operational limits. Observing the safety factors and the life expectancy of both bearings it is very clear that, from a mechanical point of view they are overdesigned; however, it is impossible to fulfill the thermally safe operation speed according to DIN 732:2010-05 with bearings of smaller size.

The design process is conducted in a qualitative to quantitative manner. The initial requirements demand the presence of five-cylinder segments: the head of the shaft where the hub is fastened with bolts onto the shaft, this is referred to as torque input, two cylinders that hold one bearing each, the cylinder that connects the two bearing and the end of the shaft which connects the shaft to the generator, this is referred to as torque output. With this initial outline, the types of bearings that are used are determined. Given the operating conditions of the bearings; low-speed, low temperature, high axial, and high radial force the best combinations possible are either two spherical roller bearings or a spherical roller bearing combined with a toroidal bearing. When trying to install a toroidal bearing with the spherical bearing the issue appears that, since the load is on the left side of the spherical roller bearing as shown in figure 4.2.1, toroidal bearings that have the appropriate size, are not submitted to enough radial load. This causes that the friction within the bearing is too low, causing slip and leading to poor operating condition, making this type of bearing unsuitable for this scenario, this leads to the use of two spherical roller bearings. The nature of this bearing set up requires one to be locating and the other to be non-locating to allow the compensation of displacements.

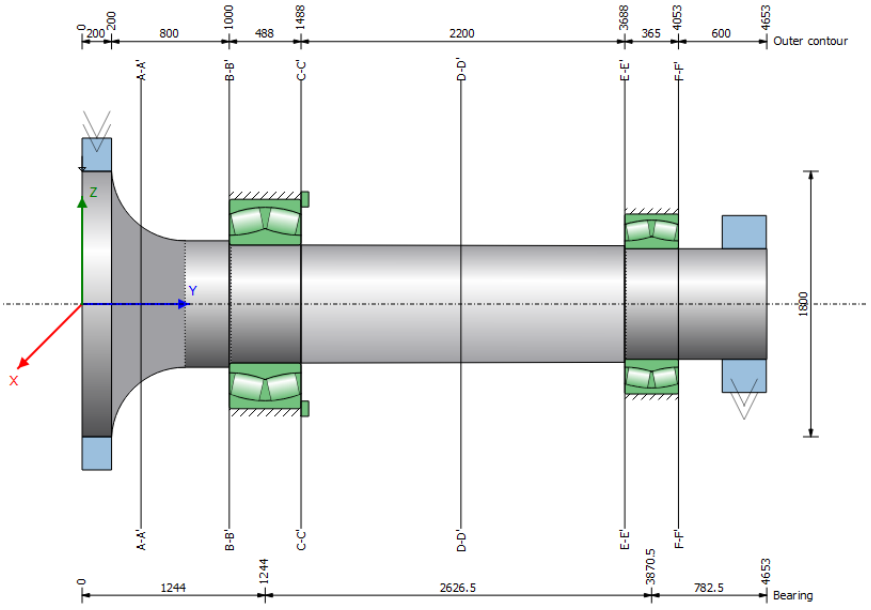

Figure 4.2.1 Shaft Layout

Selected the bearings the loads are applied, and the sizing process begins. Once the correct cylinder diameter and bearings are fitted, table 4.2.1. The section-changing radii are fitted according to the requirements given by the manufacturer SKF and the resistance for fatigue is calculated. This leads to the following security coefficients along the most critical sections as specified in Table 4.2.2 and bearing life in Table 4.2.3. A complete drawing of the shaft can be found in Appendix 7.2. Since the second bearing can be significantly smaller than the first one and to ease the assembly of the first one the middle

sector is given a conical shape. The limiting factor now starts to be the fatigue resistance of the shaft, that limits the further reducing in size.

Table 4.2.1 Loads onto the shaft

Thrust	1000 kN
Weight	95 T
Torque	5500 kNm

Table 4.2.2 Sized Bearings

Bearing	D_0 (mm)	B (mm)	p_{min} (kN)
SKF 232/800 CAF/W33	800	488	430
SKF 231/750 CA/W33	750	365	290

As mentioned earlier on, the critical part about bearings in these operating conditions is not the load state itself, but the temperature, friction, and indispensable appropriate lubrication. Therefore, the selected bearings are analyzed in detail with the SKF bearing tool. With this tool proper lubrication is selected to ensure correct values for the viscosity ratio κ, the speed factor, and the fulfilling of minimum loads is checked. This then provides the relubrication periods.

Results of the Kisssoft analysis of the shaft. Figure 4.2.1 shows the 2D layout of the shaft and distances of the final design. The sections A-A’ up to F-F’ are expected to be the most critical ones in terms of stress so they are analyzed in more detail and checked for statical and fatigue safety factors in those areas. The results are, using as material for the shaft 18CrNiMo7-6 considering that the equivalent stress evolves along the shaft as shown in Figure 4.2.2 are listed in Table 4.2.3. The overall criteria established by the NREL demands for the safety coefficients to follow the IEC 61400 guidelines therefore, above 2.6 for statics and above 1.5 for fatigue. As for all critical areas fulfill these conditions, this part is determined to be accomplished. The displacement of the shaft is shown in Figure 4.2.3.

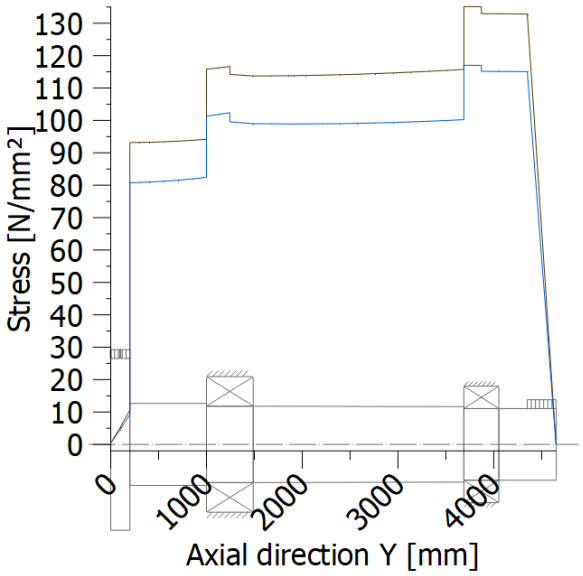

Figure 4.2.2 Equivalent Stress according to Mises and Tresca along the shaft

Table 4.2.3 Safety Factors in the critical sections

Section	Static	Fatigue
A-A’	4.36	4.09
B-B’	3.49	2.05
C-C’	3.46	3.24
D-D’	2.91	1.75
E-E’	2.91	2.74
F-F’	3.45	3.24

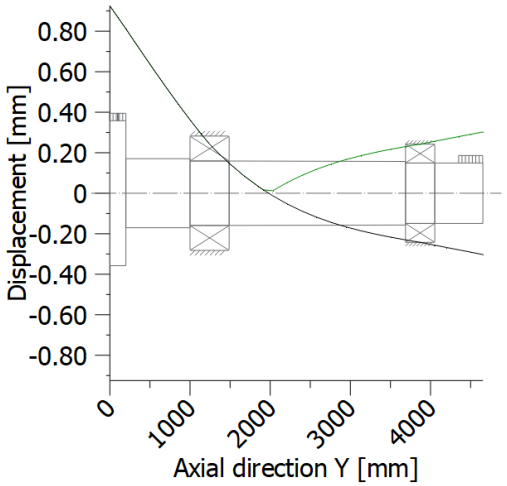

Figure 4.2.3 Deformation of the shaft

For the bearings, as mentioned previously, Kisssoft indicates a certain lifetime, Table 4.2.4, however adverts that thermal conditions need to be controlled and that is done with the SKF tool. Introducing the type of bearings, loading state and distance into the bearing tool, this can be deduced.

Table 4.2.4 Bearing Results given by Kisssoft

Bearing	Static Safety	Lifetime (h)	Allowable misalignment (mrad)	Misalignment (mrad)
SKF 232/800 CAF/W33	12.31	266487	61.09	0.433
SKF 231/750 CA/W33	82.33	>1000000	52.36	0.078

Table 4.2.5 Bearing Losses due to the Bearings.

Bearing	Torque Loss (Nm)	Power Loss (W)
SKF 232/800 CAF/W33	1015.42	2977.38
SKF 231/750 CA/W33	37.35	109.52

Tables 4.2.6, and 4.2.7 show the results gathered using the SKF tool for lubrication and thermal operating conditions.

Table 4.2.6

Bearing	Static Safety	Lifetime (h)	Speed Factor (mm/min)	C/P	Dm (mm)
SKF 232/800 CAF/W33	12.6	>200000	61.09	6.34	1110
SKF 231/750 CA/W33	64.5	>200000	52.36	36.71	985

Using the two diagrams given in Figure 4.2.4, the required viscosity of operation is determined and introduced into the SKF to complete lubrication. Since the d_m is 1110 for the first bearing and 985 for the second one and the operating maximum speed is 28 revolutions per minute this gives a rated viscosity of approximately 100 milimetres squared per second. Given maximum operational temperatures around 70 degrees Celsius, the ISO VG required is above the 460 line, therefore, for safety, ISO VG 680 should be used. This leads to the results reagarding lubrication exposed in Table 4.2.7.

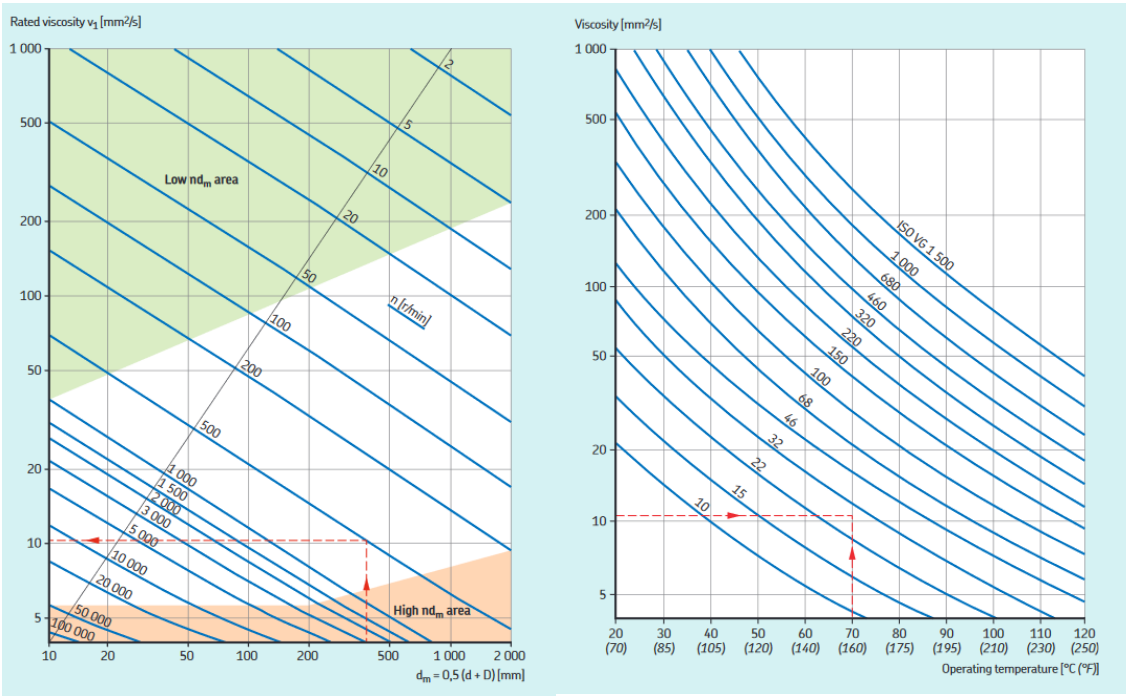

Figure 4.2.4 [8] Selection charts for lubrication

Table 4.2.7

Bearing	Viscosity Ratio κ	Relubrication period (h)	Power Loss (W)
SKF 232/800 CAF/W33	1.66	1520	5666
SKF 231/750 CA/W33	1.55	8750	570

A value of κ between one and four indicates mixed lubrication, i.e., reduced contact of rough surfaces, ideal value to prolong bearing life without incurring into major friction losses that would lead to slip.

For assembly, the recommended fits by SKF for each bearing therefore is represented in Table 4.2.8.

Table 4.2.8

Bearing	Shaft	Housing
SKF 232/800 CAF/W33	r7	G7
SKF 231/750 CA/W33	r7	G6

4.3 Sizing of the bolts to connect hub to shaft

As the shaft in a horizontal position, the weight of the assembly of hub and blades acts on the bolt as pure shear stress. The magnitude of this load is ninety tones, which is, as mentioned previously a combination of the three blades, and estimated hub weight times a security coefficient of one point two. As the center of mass of the assembled hub is outside the disk this causes a bending momentum that adds tensile/compressive loading to the bolts. Since the design of the hub is not part of this project the distance is conservatively estimated to be five meters. Therefore, the loads are listed in table 4.3.1.

Table 4.3.1 Loads for bolts

Shear (kN)	950
Bending (kNm)	4750

To perform the sizing using the bolting pattern the centroid of the pattern and the moments of inertia along the axis at the centroid are calculated. By design it is going to be enforced that all bolts are the same size and that the pattern is symmetrical along both axes, thus, the centroid remains in the center of the disk. Transposing the moment of inertia onto the centroid with equation 4.3.1.

$$I_x = I_y = A \times \sum r_{x,y}^2 \qquad \text{(Eq 4.3.1)}$$

Using a rough sizing of the area to support the bending moment it would require 24 bolts M45. Using a layout of 24 the Von Mises as a function of the area of each individual bolt can be used to determine the metric in equation 4.3.2.

$$\sigma = \sqrt{\left(1.2\frac{4750000 \times 1000 \times 900}{8.67 \times 10^6 A}\right)^2 + 3\left(1.2\frac{950000}{24A}\right)^2} \qquad \text{(Eq 4.3.2)}$$

Equaling equation 4.3.2 to the yield limit given to grade 8.8 bolts of six hundred megapascals, it is determined that 24 M42 bolts accomplish this criterion. This is based on the table contained in figure 4.3.1.

PROPERTIES OF GRADE 8.8 BOLT & NUT (ISO)

BOLT SIZE	PITCH	STRESS AREA MM2	BOLT/STUD/SCREW ISO 898-1 Gr.8.8						NUT ISO 898-2 Gr.8		
			PROOF STRESS N/MM2	PROOF LOAD KN	TENSILE STRESS N/MM2	TOUR-QUE* N-m	HARD-NESS HRC	ELONGA-TION# %	PROOF STRESS N/MM2	PROOF LOAD KN	HARD-NESS HRC
M6	1	20.1	580	11.7	800.0	9.4	22-32	12.0	855	17.2	30 Max
M8	1.25	36.6	580	21.2	800.0	22.8	22-32	12.0	870	31.8	30 Max
M10	1.5	58.8	580	34.1	800.0	45.8	22-32	12.0	880	51.7	30 Max
M12	1.75	84.3	580	48.9	800.0	78.8	22-32	12.0	880	74.2	38 Max
M14	2.0	115.0	580	66.7	800.0	125.4	22-32	12.0	880	101.2	38 Max
M16	2.0	157.0	580	91.1	800.0	195.6	22-32	12.0	920	144.4	38 Max
M18	2.5	192.0	600	115.2	830.0	278.4	23-34	12.0	920	176.6	38 Max
M20	2.5	245.0	600	147.0	830.0	394.7	23-34	12.0	920	225.4	38 Max
M22	2.5	303.0	600	181.8	830.0	536.9	23-34	12.0	920	278.8	38 Max
M24	3.0	353.0	600	211.8	830.0	682.4	23-34	12.0	920	324.8	38 Max
M27	3.0	459.0	600	275.4	830.0	998.3	23-34	12.0	920	422.3	38 Max
M30	3.5	561.0	600	336.6	830.0	1,356	23-34	12.0	920	516.1	38 Max
M33	3.5	694.0	600	416.4	830.0	1,845	23-34	12.0	920	638.5	38 Max
M36	4.0	817.0	600	490.2	830.0	2,369	23-34	12.0	920	751.6	38 Max
M39	4.0	976.0	600	585.6	830.0	3,066	23-34	12.0	920	897.9	38 Max
M42	4.5	1,120.0	600	672.0	830.0	3,789	23-34	12.0	920	1,030.4	38 Max
M45	4.5	1,310.0	600	786.0	830.0	4,748	23-34	12.0	920	1,205.2	38 Max
M48	5.0	1,470.0	600	882.0	830.0	5,684	23-34	12.0	920	1,352.4	38 Max
M52	5.0	1,760.0	600	1,056.0	830.0	7,732	23-34	12.0	920	1,619.2	38 Max
M56	5.5	2,030.0	600	1,218.0	830.0	9,157	23-34	12.0	920	1,867.6	38 Max
M60	5.5	2,360.0	600	1,416.0	830.0	11,406	23-34	12.0	920	2,171.2	38 Max
M64	6.0	2,680.0	600	1,608.0	830.0	13,816	23-34	12.0	920	2,465.6	38 Max
M68	6.0	3,060.0	600	1,836.0	830.0	16,761	23-34	12.0	920	2,815.2	38 Max
M72	6.0	3,460.0	600	2,076.0	830.0	20,067	23-34	12.0	920	3,183.2	38 Max

Figure 4.3.1 Properties of Grade 8.8 Bolts and Nuts [9]

5. Design of the shaft holder

Having finished the rotor blades and the main shaft. It is now for the requirements to fit the proper casing around these elements. This element connects the shaft through the bearings onto the Nacelle. Important requirements are assigning properly the elements that locate or not the bearing. Thus, bearing 1, which receives the axial load is located and therefore set-in place on all its moving points, bearing 2 however, needs to compensate for possible displacements through heat and must have one of its displacements open for moving. Although the bearings are fit with interference and given their size, they would not need extra fixture, a bearing cap is set on the left side with a thermal extension gap on the right bearing, to prevent major damages on the rest of the turbine in case of bearing failure. Figure 5.1 shows a longitudinal cut of the size of the bearing casing. The selected material for the bearing case is grey cast iron according to DIN-EN 1561, considering the stress analysis in figure 5.3 anything above a 250 series is enough.

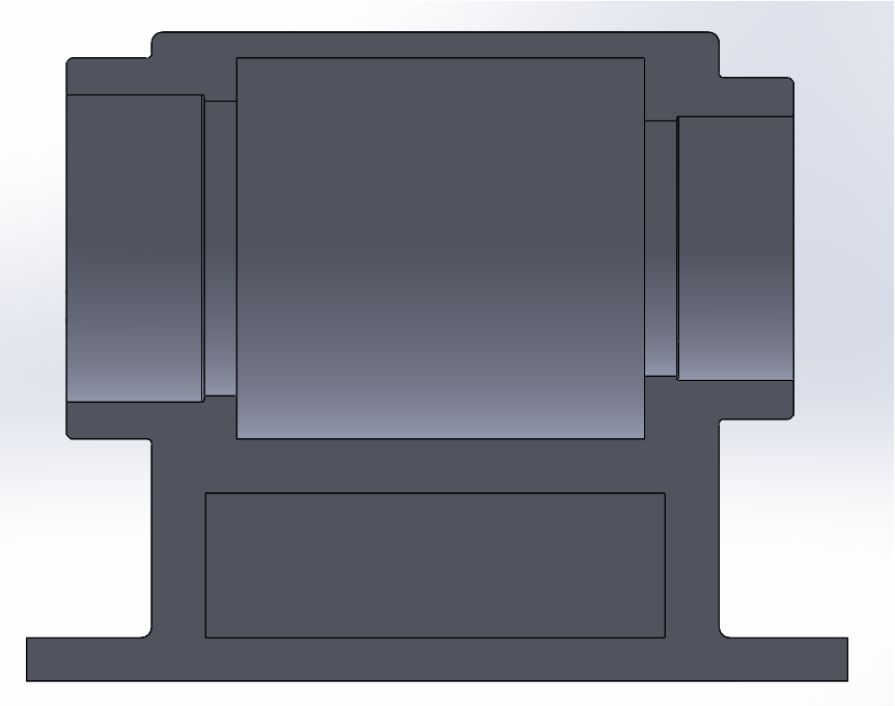

Figure 5.1 CAD Cross-section of the bearing casing

For dimensioning the bearing caps, the cap on the left is designed to purely be held in place while the right cap is designed to hold the entirety of the axial load in case of failure. Applying the same methodology as in chapter 4.3.1. The weight of the right cap is 1084kg. Using equation 5.1 the product of number of bolts and area is calculated.

$$\sigma = \sqrt{\left(1.2\frac{1000000}{nA}\right)^2 + 3\left(1.2\frac{1084}{nA}\right)^2}\ 600 \rightarrow nA = 5574 \quad \text{(Eq 5.1)}$$

Going back to figure 4.3.1 for the product of number times area there are several options. To find balance between quantity and size, 16 bolts M24x180 are chosen.

After that being designed the housing is analyzed via FEM method. The equivalent bearing loads are introduced, and the boundary condition is set that the lower part is fixed. The results are shown in Figure 5.3.

For the design of the closing cap there is an additional restriction to just the resistance criteria which is the limitation of bearing if, in case of an accident they made contact. Thus, the inner diameter of the holding segment must not exceed 1180mm.

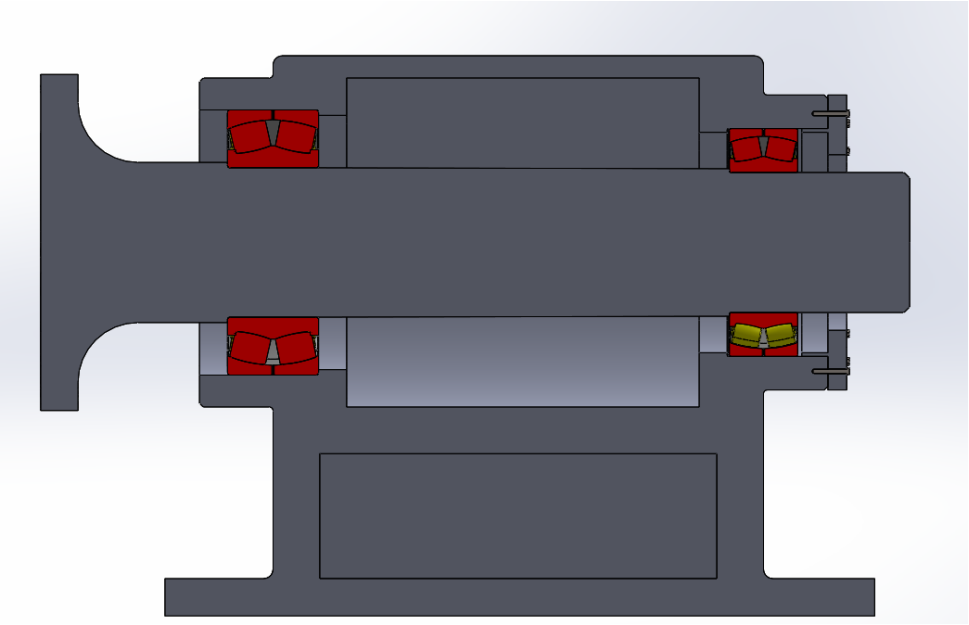

Figure 5.2 Cross-Section of the Final Shaft Assembly

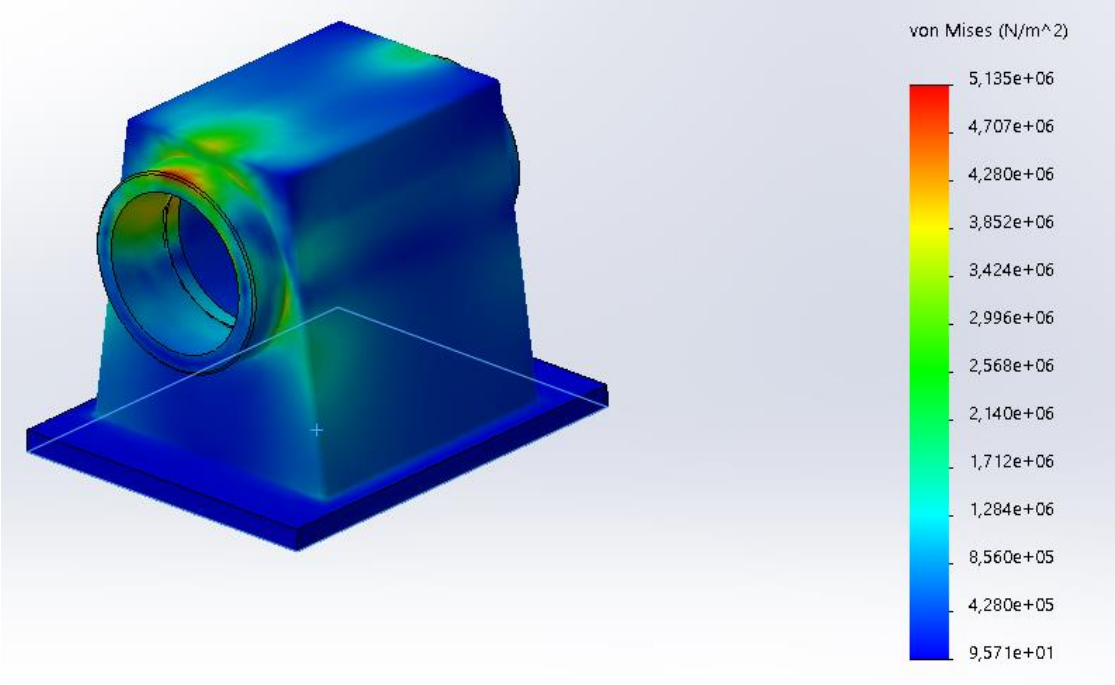

Figure 5.3 Stress Analysis on the bearing housing

6. Budget

The cost of the shaft and the bearing housing are determined by software estimation of the machining cost plus the material cost. The rest of the components are estimated with the textbook deduction from the T. Corke book mentioned in the sources. Unitary cost is listed in table 6.1

Bearing cost is determined.

$$C_B = 35{,}2 \times M_B \quad \text{(Eq 6.1)}$$

Permanent Magnet Direct Drive Generator

$$C_G = 219{,}33 \times P_R \quad \text{(Eq 6.2)}$$

Nose Cone Cost

$$C_G = 5{,}57 \times M_C \quad \text{(Eq 6.3)}$$

Hub Cost

$$C_H = 5680{,}6 + M_H \quad \text{(Eq 6.4)}$$

Pitch System Cost

$$C_P = 0{,}4801 D^{2{,}6578} \quad \text{(Eq 6.5)}$$

Blade Cost

$$C_{Bl} = 3{,}225 R^{2{,}879} \quad \text{(Eq 6.6)}$$

Labor Cost

$$C_L = 0.04019 R^3 - 21051 \quad \text{(Eq 6.7)}$$

Table 6.1 Unitary Cost table

Element	~ Unitary Cost ($)
Blade	472000
Blade Labor	-
Hub	30100
Nose Cone	10000
Shaft	287000
Generator	1900000
Bearing 1	115000
Bearing 2	61000
Bearing Housing	167000

7. Conclusions

After finishing the project up to this point there are several aspects that need addressing. First, the wind possibilities. The Spanish geography presents a high wind energy density along essentially all its coasts and is therefore, optimal for projects like offshore windfarms, some inconvenienced could be occasioned by the wind being not almost a constant flow but rather in gusts. When it comes to the rotor, it is quickly detectable that selecting the appropriate airfoil sections it is possible to extracted energy from the wind operating close to Betz limit, it might however rise the debate at what speeds the stresses and therefore the wear of the system is so high that it might be more profitable to not operate the turbine. Finally, when it comes to the transmission, the higher the rated power of the turbine the more recommendable direct drive systems are.

8. Appendixes

8.1 Planes and technical documents

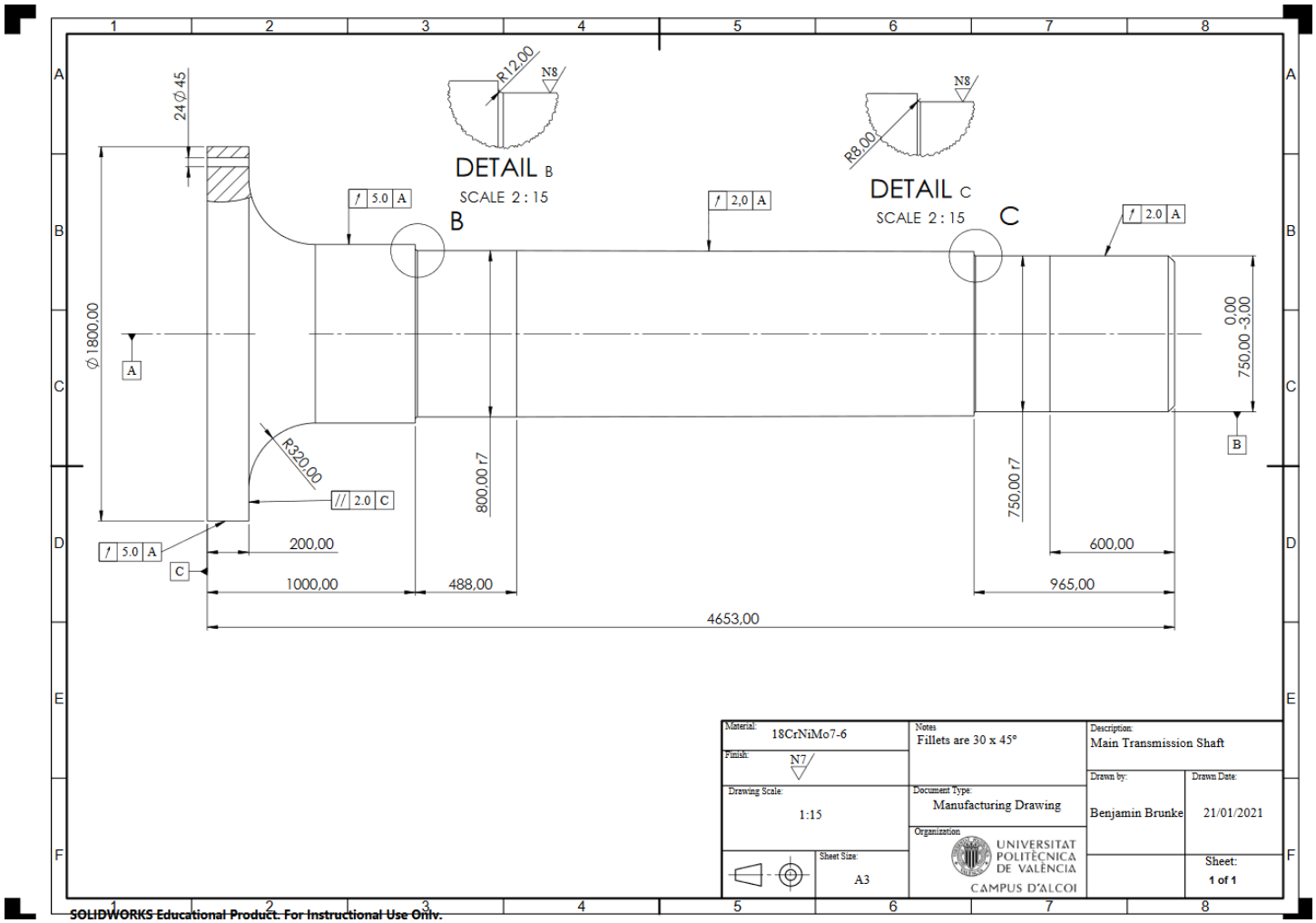

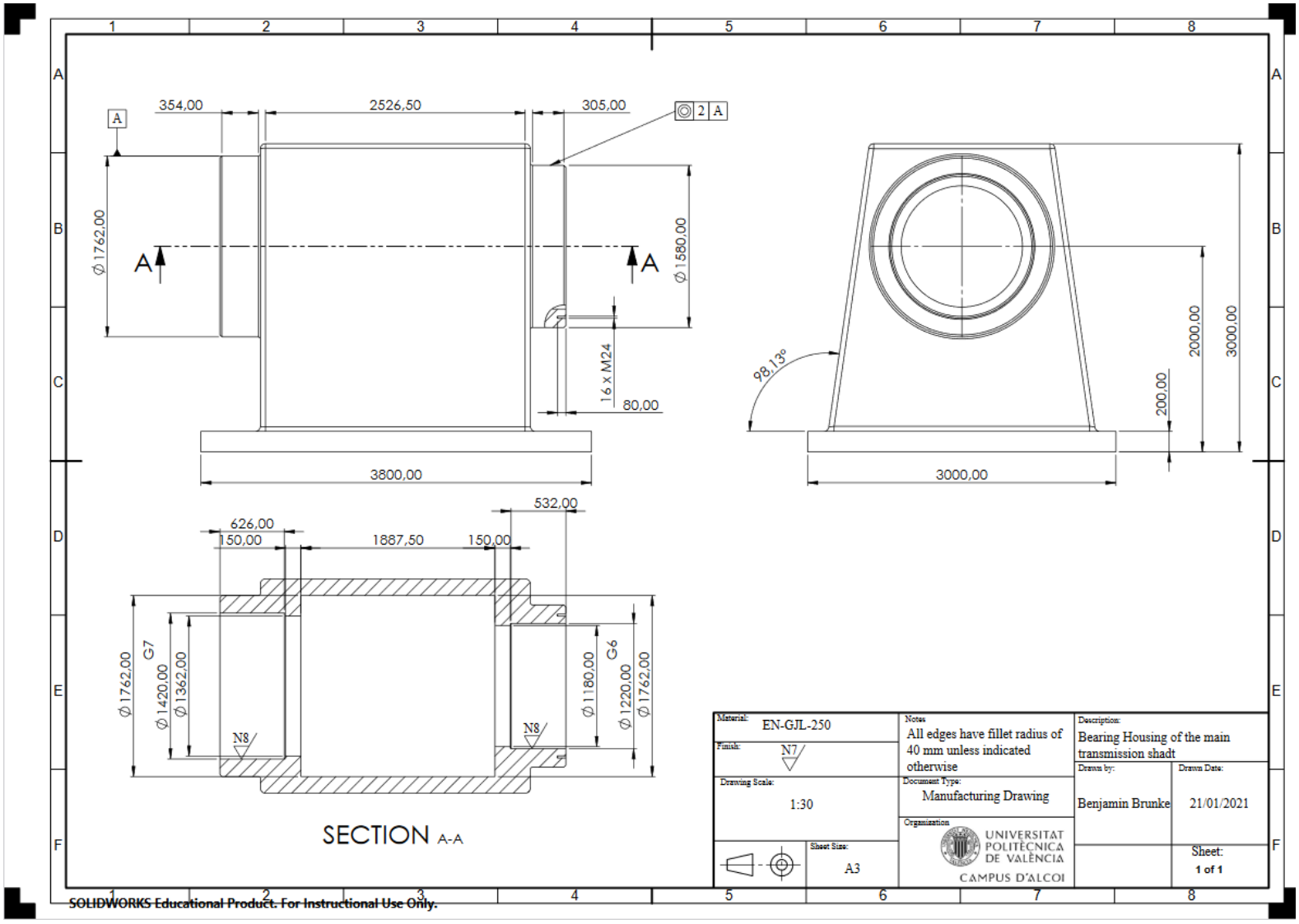
354,00
2526,50
305,00
2 A
A
Ø1762,00
Ø1580,00
16 x M24
80,00
3800,00
98,13°
2000,00
3000,00
200,00
3000,00
532,00
626,00
150,00
1887,50
150,00
Ø1762,00
G7
Ø1420,00
Ø1362,00
N8
N8
Ø1180,00
G6
Ø1220,00
Ø1762,00
SECTION A-A
Material: EN-GJL-250
Finish: N7
Drawing Scale: 1:30
Sheet Size: A3
Notes: All edges have fillet radius of 40 mm unless indicated otherwise
Document Type: Manufacturing Drawing
Organization: UNIVERSITAT POLITÈCNICA DE VALÈNCIA CAMPUS D'ALCOI
Description: Bearing Housing of the main transmission shadt
Drawn by: Benjamin Brunke
Drawn Date: 21/01/2021
Sheet: 1 of 1
SOLIDWORKS Educational Product. For Instructional Use Only.

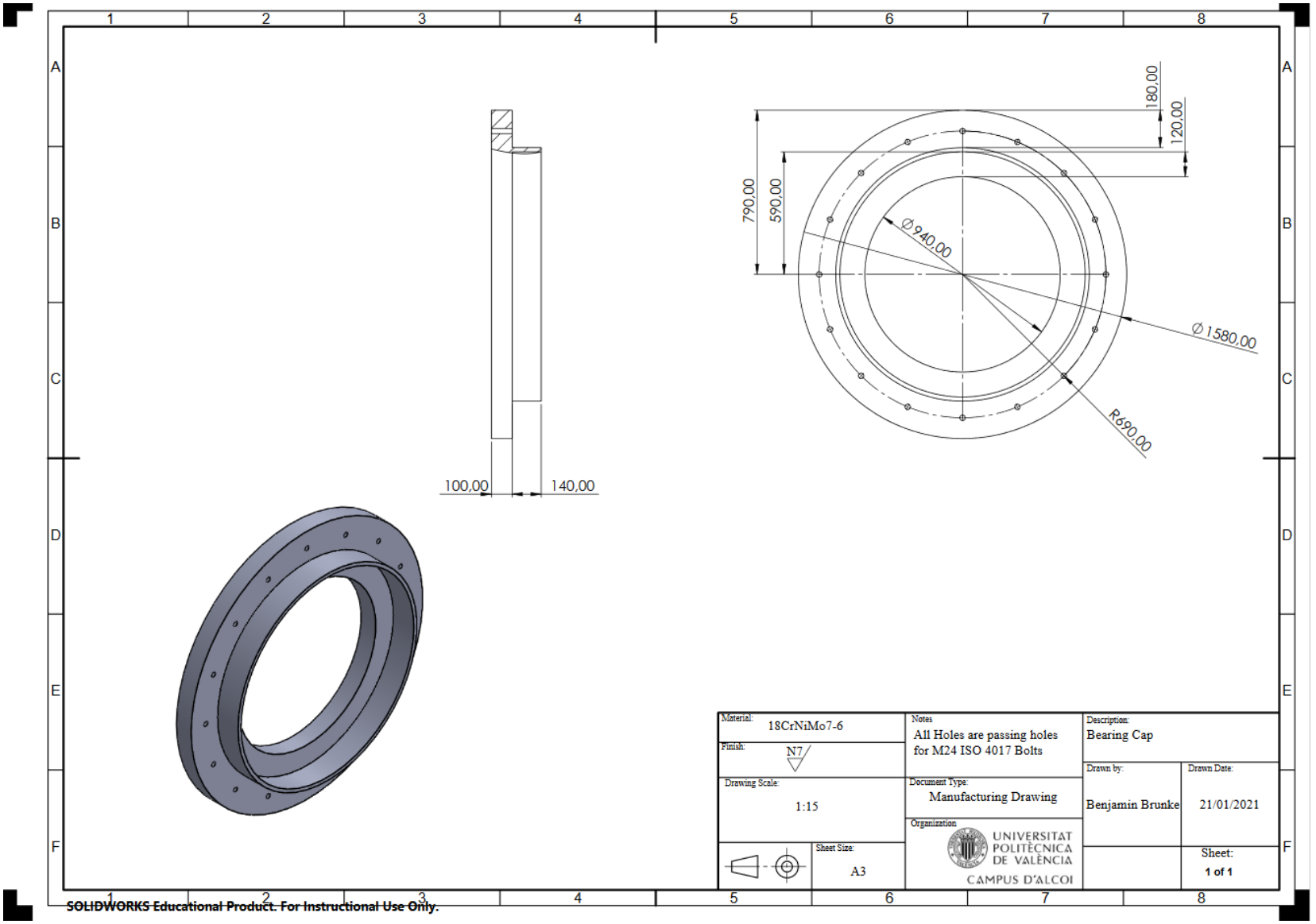

8.2 References and Sources

Citations:

[1] Europarc Spain. Yearbook 2016 – the state of protected Areas in Spain. Retrieved from https://www.europarc.org/news/2017/06/protected-areas-in-spain/

[2] Aymamí, J., García, A., Lacave, O., Lledó, LL., Mayo, M., Pares, S. (2011). Análisis del recurso. Atlas eólico de España. Estudio Técnico PER 2011 – 2020. Madrid, Spain. Meteosim Truewind.

[3] Statistic database of the Maritime Traffic. Retrieved from https://www.marinetraffic.com/

[4] Saheb, D., Koussa, M., Hadji, S. (2014). Technical and economical study of a Stand-alone Wind Energy System for Remote Rural Area Electrification in Algeria. Centre de dévéloppment des énergies renouvables. Retrieved from https://www.researchgate.net/figure/Typical-surface-roughness-lengths_tbl1_316971044

[5] Musial, W., Butterfield, C. Using Partial Safety Factors in Wind Turbine Design and Testing. (1997). National Renewable Energy Laboratory. Austin, Texas, USA. Retrieved from https://www.nrel.gov/docs/legosti/old/23257.pdf

[6] Jonkman, J., Butterfield, S., Musial, W. and Scott. G. (2009). Definition of a 5-MW Reference Wind Turbine for Offshore System Development. Retrieved from https://www.nrel.gov/docs/fy09osti/38060.pdf

[7] Lee, J.K., Park, J.Y., Oh, K.Y., Ju, S. (2015) Transformation algorithm of wind turbine blade moment signals for blade condition monitoring. Retrieved from https://www.researchgate.net/figure/Failure-rate-of-wind-turbine-components-1_fig1_276841089

[8] SKF Group 2018. (2018). *Rolling Bearings*. PUB BU/P1 17000/1 EN

[9] Rockside Export Limited. *Properties of Grade 8.8 Bolt & Nut (ISO).* Retrieved from http://rocksideltd.co.uk/PDFS/23-GRADE%208.8%20BOLT%20&%20NUT%20(ISO).pdf

Books:

- Corke, T. and Nelson R. (2018). *Wind Energy Design.* Boca Raton, FL, USA: Taylor & Francis Group, LLC.
- Stull, R.B. (1988). *An Introduction to Boundary Layer Meteorology.* Dordrecht, The Netherlands: Kluwer Academic Publishers.
- Riegels, F.W. (1958). *Aerofoil sections. Results from Wind-Tunel Investigations. Theoretical Foundations* (D. G. Randall, Translated from German.). London, United Kingdom: Butterworths.
- Taylor, D. (1996). Wind Energy. In Boyle G., *Renewable Energy. Power for a Sustainable Future* (pp. 267 – 314). Milton Keynes, United Kingdom: The Open University
- Budynas, R.G. and Nisbett J.K. (2008). *Shigley's Mechanical Engineering Design Ninth Edition.* New York, NY, USA: The McGraw-Hill Companies, Inc.

Articles/Dissertations:

- Rawson, A., Rogers, E. (2015). Assessing the impacts to vessel traffic from offshore wind farms in the Thames Estuary. *Scientific Journals of the Maritime University of Szczecin, 43(115)*, 99 – 107.
- Gryning, S.E., Batchvarova, E., Brümmer, B. and Jørgesen, H. E. (2007). On the extension of the wind profile over homogeneous terrain beyond the surface boundary layer. Retrieved from https://www.researchgate.net/publication/227021596_On_the_extension_of_the_wind_profile_over_homogeneous_terrain_beyond_the_surface_layer
- Peña, A., Floors, R., Sathe, A., Gryning, S. E., Wagner, R., Courtney, M. S., Larsén, X. G., Hahmann, A. N. and Hasager, C. B. (2015). Ten Years of Boundary-Layer and Wind-Power Meteorology at Hoevsoere, Denmark. Retrieved from https://www.researchgate.net/publication/282611368_Ten_Years_of_Boundary-Layer_and_Wind-Power_Meteorology_at_Hovsore_Denmark
- Prasad, K. S., Krishna, V. and Ashok Kumar, B. B. (2013). Aerofoil Profile Analysis and Design Optimisation. *STM Journals Volume 3, Issue 2, ISSN: 2231-0.38X*. Retrieved from https://www.researchgate.net/publication/279186627_Aerofoil_Profile_Analysis_and_Design_Optimisation
- Van de Kaa, G., Van Ek, M., Kamp, L.M., Rezaei, J. (2020). Wind turbine technology battle; Gearbox versus direct drive – opening up the black box of technology characteristics. Retrieved from https://www.researchgate.net/publication/339335797_Wind_turbine_technology_battles_Gearbox_versus_direct_drive_-opening_up_the_black_box_of_technology_characteristics
- Polinder, H. Member, IEEE, Van der Pijl F.F.A., de Vilder G, Tavner, P.J. (2006). Comparison of Direct-Drive and Geared Generator Concepts for Wind Turbines. Retrieved from https://www.researchgate.net/publication/3270581_Comparison_of_Direct-Drive_and_Geared_Generator_Concepts_for_Wind_Turbines
- Htun, Z.M., Ya, A.Z., Ma, W.M. (2017). Design and Analysis of Low Speed Direct-Drive Permanent Magnet Generator for Wind Power Application. Retrieved from https://www.researchgate.net/publication/319009776_Design_and_Analysis_of_Low_Speed_Direct-Drive_Permanent_Magnet_Generator_for_Wind_Power_Application
- Sopanen, J., Ruuskanen, V., Nerg, J., Pyrhönen, J. (2011). Dynamic Torque Analysis of a Wind Turbine Drive Train including a Direct-Driven Magnet Generator. Retrieved from https://www.researchgate.net/publication/224182558_Dynamic_Torque_Analysis_of_a_Wind_Turbine_Drive_Train_Including_a_Direct-Driven_Permanent-Magnet_Generator
- Lee, J., Park, J., Oh, K., Ju, S. (2015). Transformation algorithm of wind turbine blade moment signals for blade condition monitoring. Retrieved from

https://www.researchgate.net/publication/276841089_Transformation_algorithm_of_wind_turbine_blade_moment_signals_for_blade_condition_monitoring#pfa

- Ragheb, A., Ragheb, M. (2010). Wind Turbine Gearbox Technologies. Retrieved from https://www.researchgate.net/publication/224137242_Wind_Turbine_Gearbox_Technologies
- Zhao, M., Ji, J.C. (2016). Dynamic Analysis of Wind Gearbox Components. Retrieved from https://www.researchgate.net/publication/295082278_Dynamic_Analysis_of_Wind_Turbine_Gearbox_Components

Commercial Elements and Catalogs

- Electrical Generator. Retrieved from https://www.ingeteam.com/indar/en-us/electric-generators/wind-generators/pc30_10_187/indar-pmg-series.aspx
- Geometry of different airfoils. Retrieved from http://airfoiltools.com/

Programs and computation software used:

- Microsoft office for the elaboration of the document
- Excel for iterative calculations of wind performance.
- Kisssoft for shaft analysis.
- SKF Tool for bearing analysis.
- Solidworks for 3D Cad models and FEM analysis.

8.3 Appendix of Tables of aerodynamic iterative calculations

Segment 1 Cylinder 1																						
a0	a'0	phi (º)	phi(rad)	alpha (º)	alpha(rad)	Cl	Cd	Cn	Ct	σr	a1	Δa	a'1	Δa'	f	F	Vr	Fn	Ft	dT	dQ	dP
0	0	69,99720919	1,221681767	56,6892092	0,98941335	0	0,5	0,46983798	-0,17103296	0,5899572	0,072768058	0,07276806	-0,07276806	0,07276806								
0,072768058	-0,07276806	69,99720919	1,221681767	56,6892092	0,98941335	0	0,5	0,46983798	-0,17103296	0,5899572	0,072768058	0	-0,07276806	0	N/A	N/A	14,8013568	1831,10977	-666,570461	1831,10977	-1910,85754	-3639,72865
Segment 2 Cylinder 1																						
0	0	54,58294472	0,952652101	41,2749447	0,72038368	0	0,5	0,40747766	-0,28976189	0,32860781	0,047984199	0,0479842	-0,0479842	0,0479842								
0,047984199	-0,0479842	54,58294472	0,952652101	41,2749447	0,72038368	0	0,5	0,40747766	-0,28976189	0,32860781	0,047984199	0	-0,0479842	0	N/A	N/A	17,5227237	2421,77278	-1722,14953	2421,77278	-9644,03739	-18369,595
Segment 3 Cylinder 2																						
0	0	43,38035691	0,757130059	30,0723569	0,52486164	0	0,35	0,24039343	-0,25438357	0,23875951	0,029518972	0,02951897	-0,02951897	0,02951897								
0,029518972	-0,02951897	43,38035691	0,757130059	30,0723569	0,52486164	0	0,35	0,24039343	-0,25438357	0,23875951	0,029518972	0	-0,02951897	6,9389E-18	N/A	N/A	21,1945284	2259,99907	-2391,52384	2259,99907	-19929,2856	-37960,544
Segment 4 DU40																						
0	0	33,83049808	0,590453579	20,5224981	0,35818516	1,76E+00	4,26E-01	1,70E+00	6,28E-01	0,18518054	0,202643865	0,20264387	6,71E-02	0,06709417								
2,03E-01	6,71E-02	26,60160138	0,46428553	13,2936014	0,23201711	1,57E+00	1,27E-01	1,46E+00	5,90E-01	0,18518054	0,252244865	0,049601	0,07324271	0,00614854								
2,52E-01	7,32E-02	25,03041353	0,436863129	11,7224135	0,20459471	1,48E+00	8,23E-02	1,38E+00	5,53E-01	0,18518054	0,262924633	0,01067977	0,07159451	0,0016482								
2,63E-01	7,16E-02	24,74935999	0,43195782	11,44136	0,1996894	1,47E+00	7,55E-02	1,36E+00	5,45E-01	0,18518054	0,264651702	0,00172707	0,07108338	0,00051113								
2,65E-01	7,11E-02	24,7086756	0,431247743	11,4006756	0,19897933	1,46E+00	7,45E-02	1,36E+00	5,44E-01	0,18518054	0,264895981	0,00024428	0,07100371	7,9671E-05								
2,65E-01	7,10E-02	24,7030657	0,431149832	11,3950657	0,19888142	1,46E+00	7,44E-02	1,36E+00	5,44E-01	0,18518054	0,264929546	3,3566E-05	0,07099261	1,1099E-05	N/A	N/A	26,3846529	3,25E+04	1,30E+04	3,25E+04	1,53E+05	290783,454
Segment 5 DU35																						
0,00E+00	0,00E+00	26,42027377	0,461120767	14,940	0,26075697	1,69E+00	1,07E-01	1,56E+00	6,56E-01	0,14014081	0,216395924	0,21639592	6,12E-02	0,06122838								
2,16E-01	6,12E-02	20,14644107	0,351621729	8,666	0,15125793	1,36E+00	2,63E-03	1,28E+00	4,66E-01	0,14014081	0,274083779	0,05768785	5,32E-02	0,00802668								
2,74E-01	5,32E-02	18,90373059	0,32993234	7,424	0,12956854	1,22E+00	1,41E-03	1,15E+00	3,93E-01	0,14014081	0,277963848	0,00388007	4,71E-02	0,00610731								
2,78E-01	4,71E-02	18,91174494	0,330072216	7,432	0,12970842	1,22E+00	1,40E-03	1,15E+00	3,94E-01	0,14014081	0,277952093	1,1755E-05	4,71E-02	4,3298E-05	N/A	N/A	33,4161157	4,52E+04	1,54E+04	4,52E+04	2,44E+05	465464,692
Segment 6 DU35																						
0,00E+00	0,00E+00	21,54097592	0,375960954	11,379	0,1986006	1,59E+00	2,57E-02	1,48E+00	5,58E-01	0,10669679	0,226995185	0,22699519	4,56E-02	0,04558369								
0,226995185	4,56E-02	16,26886883	0,283945327	6,107	0,10658497	1,05E+00	4,65E-03	1,01E+00	2,89E-01	0,10669679	0,254764312	0,02776913	2,95E-02	0,01610565								
0,254764312	2,95E-02	15,94721722	0,278331447	5,785	0,10097109	1,00E+00	5,93E-03	9,65E-01	2,70E-01	0,10669679	0,254229838	0,00053447	2,80E-02	0,00150516								
0,254229838	2,80E-02	15,98024574	0,278907903	5,818	0,10154754	1,01E+00	5,80E-03	9,69E-01	2,71E-01	0,10669679	0,254301856	7,2018E-05	2,81E-02	0,00015622								
0,254301856	2,81E-02	15,97647727	0,278842131	5,814	0,10148177	1,01E+00	5,81E-03	9,69E-01	2,71E-01	0,10669679	0,254293842	8,0146E-06	2,81E-02	1,7806E-05	N/A	N/A	40,6385807	5,37E+04	1,50E+04	53722,3511	3,00E+05	571702,417
Segment 7 DU30																						
0	0	18,13066295	0,316439764	9,120	0,15916815	1,34E+00	1,45E-02	1,28E+00	4,04E-01	0,08435792	0,218158311	0,21815831	2,97E-02	0,02968497								
0,218158311	2,97E-02	13,96223076	0,243686898	4,951	0,08641528	9,69E-01	4,13E-03	9,41E-01	2,30E-01	0,08435792	0,254297014	0,0361387	2,11E-02	0,00855064								
0,254297014	2,11E-02	13,44812675	0,23471409	4,437	0,07744247	9,07E-01	5,22E-03	8,83E-01	2,06E-01	0,08435792	0,256099919	0,0018029	1,96E-02	0,00157424								
0,256099919	1,96E-02	13,43675515	0,234515618	4,426	0,077244	9,05E-01	5,24E-03	8,82E-01	2,05E-01	0,08435792	0,256129283	2,9364E-05	1,95E-02	3,584E-05	N/A	N/A	48,0200132	6,51E+04	1,51E+04	65063,6834	3,64E+05	693967,309
Segment 8 DU25																						
0	0	15,62903379	0,272778099	7,834	0,13672968	1,24E+00	1,68E-02	1,20E+00	3,19E-01	0,06796654	0,219702152	0,21970215	2,13E-02	0,02133881								
0,219702152	2,13E-02	12,06423733	0,210560663	4,269	0,07451225	9,94E-01	4,45E-03	9,73E-01	2,03E-01	0,06796654	0,274570769	0,05486862	1,72E-02	0,0041365								
0,274570769	1,72E-02	11,28281352	0,196922245	3,488	0,06087383	9,18E-01	4,10E-03	9,01E-01	1,76E-01	0,06796654	0,285678343	0,01110757	1,58E-02	0,00140848								
0,285678343	1,58E-02	11,12941409	0,19424492	3,334	0,0581965	9,02E-01	4,10E-03	8,86E-01	1,70E-01	0,06796654	0,287744288	0,00206594	1,55E-02	0,00029784								
0,287744288	1,55E-02	11,10120027	0,193752496	3,306	0,05770408	8,99E-01	4,11E-03	8,83E-01	1,69E-01	0,06796654	0,288119225	0,00037494	1,54E-02	5,554E-05	N/A	N/A	55,4881878	8,21E+04	1,57E+04	81925,7771	4,42E+05	842644,713
Segment 9 DU25																						
0	0	13,72229713	0,239499266	7,178	0,12528492	1,21E+00	1,29E-02	1,18E+00	2,74E-01	0,05549119	0,225098326	0,22509833	1,68E-02	0,01679587								
0,225098326	1,68E-02	10,54184432	0,183989893	3,998	0,06977555	9,69E-01	4,25E-03	9,53E-01	1,73E-01	0,05549119	0,283139112	0,05804079	1,35E-02	0,0032708								
0,283139112	1,35E-02	9,798970603	0,1710243	3,255	0,05680995	8,94E-01	4,11E-03	8,81E-01	1,48E-01	0,05549119	0,296823358	0,01368425	1,24E-02	0,00112715								
0,296823358	1,24E-02	9,625947307	0,168004474	3,082	0,05379013	8,75E-01	4,16E-03	8,64E-01	1,42E-01	0,05549119	0,299949564	0,00312621	1,21E-02	0,00028255								
0,299949564	1,21E-02	9,586573333	0,167317269	3,043	0,05310292	8,71E-01	4,17E-03	8,59E-01	1,41E-01	0,05549119	0,300656337	0,00070677	1,21E-02	6,5351E-05	N/A	N/A	63,0533359	9,65E+04	1,58E+04	96162,7342	5,10E+05	971905,788

Segment 10 DU21																						
a0	a'0	phi (º)	phi(rad)	alpha (º)	alpha(rad)	Cl	Cd	Cn	Ct	σr	a1	Δa	a'1	Δa'	f	F	Vr	Fn	Ft	dT	dQ	dP
0	0	12,22386805	0,213346745	6,863	0,11977964	1,20E+00	1,08E-02	1,18E+00	2,44E-01	0,04600086	0,231716888	0,23171689	1,37E-02	0,01372945								
0,231716888	1,37E-02	9,324171544	0,162737493	3,963	0,06917039	9,98E-01	5,10E-03	9,85E-01	1,57E-01	0,04600086	0,301477175	0,06976029	1,14E-02	0,00233764								
0,301477175	1,14E-02	8,509812189	0,148524241	3,149	0,05495714	9,23E-01	4,95E-03	9,14E-01	1,32E-01	0,04600086	0,324331922	0,02285475	1,05E-02	0,00093061								
0,324331922	1,05E-02	8,242744715	0,143863035	2,882	0,05029593	8,97E-01	5,01E-03	8,89E-01	1,24E-01	0,04600086	0,332161874	0,00782995	1,01E-02	0,00033198								
0,332161874	1,01E-02	8,151156236	0,142264514	2,790	0,04869741	8,88E-01	5,03E-03	8,80E-01	1,21E-01	0,04600086	0,334885494	0,00272362	1,00E-02	0,00011691	7,75627901	0,99975046	70,6531996	1,16E+05	1,59E+04	114476,551	5,86E+05	1115684,81
Segment 11 DU21																						
0	0	11,01680969	0,192279602	6,829	0,11918521	1,20E+00	1,06E-02	1,18E+00	2,19E-01	0,0384344	0,236729615	0,23672962	1,13E-02	0,01132706								
0,236729615	1,13E-02	8,358819513	0,145888922	4,171	0,07279453	1,02E+00	5,21E-03	1,01E+00	1,42E-01	0,0384344	0,313667415	0,0769378	9,61E-03	0,00172096								
0,313667415	9,61E-03	7,539120739	0,13158248	3,351	0,05848809	9,43E-01	4,95E-03	9,35E-01	1,19E-01	0,0384344	0,342936791	0,02926938	8,85E-03	0,00075513								
0,342936791	8,85E-03	7,226422969	0,126124874	3,038	0,05303048	9,13E-01	4,97E-03	9,06E-01	1,10E-01	0,0384344	0,354954148	0,01201736	8,53E-03	0,00031733								
0,354954148	8,53E-03	7,097824725	0,123880411	2,910	0,05078602	9,00E-01	5,00E-03	8,94E-01	1,06E-01	0,0384344	0,360043872	0,00508972	8,40E-03	0,00013527	6,76749613	0,99928171	78,3051963	1,34E+05	1,60E+04	131422,228	6,56E+05	1250424,23
Segment 12 NACA64																						
0	0	10,0244868	0,1749603	6,899	0,12041876	7,84E-01	3,58E-02	7,78E-01	1,01E-01	0,03226064	0,171523012	0,17152301	4,78E-03	0,00477926								
0,171523012	4,78E-03	8,292546462	0,144732239	5,168	0,0901907	5,08E-01	3,53E-02	5,08E-01	3,83E-02	0,03226064	0,164425163	0,00709785	2,17E-03	0,00260799								
0,164425163	2,17E-03	8,384044419	0,14632918	5,259	0,09178764	5,23E-01	3,51E-02	5,22E-01	4,15E-02	0,03226064	0,165395053	0,00096989	2,32E-03	0,00015254								
0,165395053	2,32E-03	8,37319432	0,14613981	5,248	0,09159827	5,21E-01	3,52E-02	5,21E-01	4,11E-02	0,03226064	0,165283764	0,00011129	2,31E-03	1,8054E-05	4,26597539	0,99097485	85,9707347	8,73E+04	6,89E+03	86539,2905	3,06E+05	583685,402
Segment 13 NACA																						
0	0	9,194743163	0,160478542	6,876	0,12000436	7,80E-01	3,58E-02	7,76E-01	8,93E-02	0,02712748	1,71E-01	0,17085465	3,86E-03	0,00385596								
1,71E-01	3,86E-03	7,615207222	0,132910439	5,296	0,09243625	5,29E-01	3,51E-02	5,29E-01	3,53E-02	0,02712748	1,70E-01	0,00122888	1,83E-03	0,00202944								
1,70E-01	1,83E-03	7,641627661	0,133371563	5,323	0,09289738	5,33E-01	3,51E-02	5,33E-01	3,62E-02	0,02712748	1,70E-01	0,00017153	1,86E-03	3,8011E-05								
1,70E-01	1,86E-03	7,639781381	0,133339339	5,321	0,09286515	5,33E-01	3,51E-02	5,33E-01	3,61E-02	0,02712748	1,70E-01	1,1806E-05	1,86E-03	2,6538E-06	3,32804887	0,97695963	93,6709191	9,74E+04	6,60E+03	9,51E+04	3,14E+05	598093,255
Segment 14 NACA																						
0	0	8,490926159	0,148194618	6,965	0,12156089	7,93E-01	3,60E-02	7,90E-01	8,14E-02	0,02279226	1,71E-01	0,17105194	3,19E-03	0,00318688								
1,71E-01	3,19E-03	7,032465684	0,122739681	5,506	0,09610596	5,64E-01	3,49E-02	5,64E-01	3,44E-02	0,02279226	1,76E-01	0,00542726	1,62E-03	0,00157064								
1,76E-01	1,62E-03	6,997727183	0,122133379	5,472	0,09549966	5,58E-01	3,49E-02	5,58E-01	3,33E-02	0,02279226	1,76E-01	3,6916E-05	1,57E-03	4,2931E-05	2,39242604	0,94132633	101,393869	1,09E+05	6,50E+03	1,02E+05	3,32E+05	631652,566
Segment 15 NACA																						
0	0	7,981277807	0,139299576	7,118	0,12423738	8,14E-01	3,66E-02	8,11E-01	7,68E-02	0,01966305	1,71E-01	0,17142786	2,75E-03	0,00275335								
1,71E-01	2,75E-03	6,608435779	0,115338963	5,745	0,10027677	6,03E-01	3,47E-02	6,03E-01	3,50E-02	0,01966305	1,83E-01	0,01147053	1,51E-03	0,00124816								
1,83E-01	1,51E-03	6,525795943	0,113896626	5,663	0,09883443	5,89E-01	3,47E-02	5,90E-01	3,25E-02	0,01966305	1,83E-01	0,00037534	1,42E-03	8,8943E-05	1,60572572	0,87071311	107,843965	7,97E+04	4,39E+03	6,92E+04	2,28E+05	434480,555
Segment 16 NACA																						
0	0	7,615350766	0,132912945	7,245	0,12645523	8,31E-01	3,71E-02	8,29E-01	7,33E-02	0,01691037	1,66E-01	0,16634161	2,37E-03	0,00236622								
1,66E-01	2,37E-03	6,345109311	0,110743049	5,975	0,10428533	6,41E-01	3,46E-02	6,41E-01	3,64E-02	0,01691037	1,81E-01	0,01512509	1,40E-03	0,00096333								
1,81E-01	1,40E-03	6,236850337	0,108853573	5,867	0,10239586	6,23E-01	3,46E-02	6,23E-01	3,33E-02	0,01691037	1,82E-01	0,00098923	1,30E-03	9,9491E-05	0,96111452	0,7493975	113,01678	8,34E+04	4,45E+03	6,21E+04	2,11E+05	402635,037
Segment 17 NACA																						
0	0	7,281333929	0,127083251	7,175	0,1252332	7,48E-01	4,06E-02	7,47E-01	5,45E-02	0,01099313	1,13E-01	0,1133356	1,19E-03	0,00119273								
1,13E-01	1,19E-03	6,455887595	0,112676495	6,350	0,11082645	6,37E-01	3,84E-02	6,38E-01	3,36E-02	0,01099313	1,22E-01	0,00842506	8,26E-04	0,0003664								
1,22E-01	8,26E-04	6,397376362	0,111655281	6,291	0,10980523	6,29E-01	3,83E-02	6,29E-01	3,20E-02	0,01099313	1,22E-01	0,00053767	7,96E-04	3,0575E-05	0,29851937	0,46720615	118,229986	6,27E+04	3,19E+03	2,92E+04	9,54E+04	1,82E+05